Chemical Geology 455 (2017) 98–119

Contents lists available at ScienceDirect

Chemical Geology

journal homepage: www.elsevier.com/locate/chemgeo

Tectonic significance and redox state of Paleoproterozoic eclogite and pyroxenite components in the Slave cratonic mantle lithosphere, Voyageur kimberlite, Arctic Canada

K.A. Smart [a,*], S. Tappe [b], A. Simonetti [c], S.S. Simonetti [c], A.B. Woodland [d], C. Harris [e]

[a] School of Geosciences, University of the Witwatersrand, Johannesburg 2001, South Africa
[b] Department of Geology, University of Johannesburg, Auckland Park 2006, South Africa
[c] Department of Civil & Environmental Engineering & Earth Sciences, University of Notre Dame, IN 46556, USA
[d] Institut für Geowissenschaften, Goethe-Universität, Frankfurt am Main D-60438, Germany
[e] Department of Geological Sciences, University of Cape Town, Rondebosch 7701, South Africa

ARTICLE INFO

Article history:
Received 30 May 2016
Received in revised form 4 October 2016
Accepted 7 October 2016
Available online 11 October 2016

Keywords:
Lithosphere formation
Subduction
Metasomatism
Mantle redox
In-situ Pb isotopes
Oxygen isotopes

ABSTRACT

Mantle-derived eclogite and pyroxenite xenoliths from the Jurassic Voyageur kimberlite on the northern Slave craton in Arctic Canada were studied for garnet and clinopyroxene major and trace element compositions, clinopyroxene Pb and garnet O isotopic compositions, and garnet $Fe^{3+}/\Sigma Fe$ contents. The Voyageur xenoliths record a wide range of pressures, but are cooler compared to mantle xenoliths derived from the nearby, coeval Jericho kimberlite. The CaO, TiO_2 and Zr contents of Voyageur eclogites increase with depth, which is also observed in northern Slave peridotite xenoliths, demonstrating 'bottom-up' metasomatic processes within cratonic mantle lithosphere.

The Voyageur eclogites have positive Eu anomalies, flat $HREE_N$ patterns, and major element compositions that are consistent with ultimate origins from basaltic and gabbroic protoliths within oceanic lithosphere. Clinopyroxene Pb isotope ratios intercept the Stacey-Kramers two-stage terrestrial Pb evolution curve at ca. 2.1 Ga, and form an array towards the host kimberlite, indicating isotopic mixing. The 2.1 Ga eclogite formation age broadly overlaps with known Paleoproterozoic subduction and collision events that occurred along the western margin of the Slave craton. Unlike the eclogites, the Voyageur pyroxenites contain garnet with distinctive fractionated $HREE_N$, sinusoidal REE patterns of calculated bulk rocks, and clinopyroxene with $^{206}Pb/^{204}Pb$ ratios that intercept the Stacey-Kramers curve at 1.8 Ga. This suggests a distinct origin as Paleoproterozoic high-pressure mantle cumulates. However, the pyroxenite Pb isotope ratios fall within the eclogite array and could also be explained by protoliths formation at ca. 2.1 Ga followed by minor isotopic mixing during mantle metasomatism. Thus, an alternative scenario involves pyroxenite formation within the mantle section of Paleoproterozoic oceanic lithosphere followed by variable metasomatism after incorporation into cratonic mantle lithosphere. This model allows for a linked petrogenesis of the Voyageur eclogites (crust) and pyroxenites (mantle) as part of the same subducting oceanic slab.

Oxygen fugacity determinations for one pyroxenite and ten eclogite xenoliths show a range of 3 log units, from −4.6 to −1.6 ΔFMQ, similar to the range observed for nearby Jericho and Muskox eclogites (ΔFMQ −4.2 to −1.5). Importantly, the northern Slave eclogite and pyroxenite mantle components are highly heterogeneous in terms of redox state provided that they range from reduced to oxidized relative to Slave peridotite xenoliths. Moreover, the Voyageur eclogites do not exhibit any trend between oxidation state and equilibration depth, which contrasts with the downward decrease in fO_2 shown by Slave and worldwide cratonic peridotite xenoliths. Our investigation of mantle eclogite and pyroxenite fO_2 reinforces the important influence of recycled mafic components in upper mantle processes, because their high and variable redox buffering capacity strongly controls volatile speciation and melting relations under upper mantle conditions.

1. Introduction

The record of the cratonic lithospheric mantle extends back to the Paleoarchean, based on a worldwide age database for peridotite xenoliths and mineral inclusions in diamonds (Pearson and Wittig, 2014; Westerlund et al., 2006; Gurney et al., 2010). Whether the cratonic

* Corresponding author.
E-mail address: Katie.smart2@wits.ac.za (K.A. Smart).

http://dx.doi.org/10.1016/j.chemgeo.2016.10.014
0009-2541/

lithospheric mantle (CLM) formed from melt-depleted peridotite in rising mantle plumes or within the oceanic lithosphere is debated (Griffin et al., 2003; Lee et al., 2011; Pearson and Wittig, 2008), with the latter model having implications for the operation of plate tectonics prior to 3 Ga. Following craton stabilization, CLM can be modified by orogenic processes along craton margins (Aulbach, 2012; Shirey et al., 2004) and by intraplate extension and associated magmatism (Menzies et al., 1993; Tappe et al., 2007; Tappe et al., 2017, 2016). Although the CLM is dominantly composed of Archean peridotite (e.g. Pearson, 1999), less abundant but ubiquitous cratonic mantle eclogite xenoliths and eclogitic mineral inclusions in diamonds generally show Meso- to Neoarchean and Paleoproterozoic ages, which overlap with orogenic events that are known from craton margins and intra-cratonic suture zones (Aulbach et al., 2009a, 2009b; Menzies et al., 2003; Richardson et al., 2001, 2004; Schmidberger et al., 2005; Shirey et al., 2002; Smart et al., 2014; Tappe et al., 2011). Consequently, the petrogenesis of cratonic mantle eclogite has been linked to the formation and subduction of oceanic lithosphere (e.g. Aulbach et al., 2002, 2016; Dongre et al., 2015; Helmstaedt and Doig, 1975; Jacob et al., 1994; Jacob, 2004; Jacob et al., 2005; Jagoutz et al., 1985; MacGregor and Manton, 1986; Pernet-Fisher et al., 2014; Riches et al., 2016; Schmidberger et al., 2007; Smart et al., 2012, 2014). Therefore, investigation of cratonic mantle eclogites may help elucidate the compositions and redox conditions of Precambrian oceanic crust and mantle (e.g. Aulbach et al., 2016; Aulbach and Viljoen, 2015; Ireland et al., 1994; Jacob et al., 2005), and allow plate tectonic recycling processes to be tracked through time (Shirey and Richardson, 2011). However, cratonic mantle eclogites are also proposed to form by lower crustal and mantle magmatic cumulate or metasomatic processes that do not involve oceanic lithosphere protoliths and subduction processing (De Stefano et al., 2009; Greau et al., 2011; Huang et al., 2012; Smyth et al., 1989; Williams et al., 2009), which has lead to a vigorous debate regarding their origins (e.g. Griffin and O'Reilly, 2007).

Eclogites and eclogitic diamond inclusions from the Slave craton in northwest Canada have ca. 1.7–2.1 Ga ages and have been linked to subduction of oceanic crust (Aulbach et al., 2009a, 2009b; Schmidberger et al., 2005, 2007; Smart et al., 2014) that accompanied Paleoproterozoic arc accretion at the western craton margin during the ca. 1.9–2.0 Ga Wopmay orogeny (Cook et al., 1999; Hildebrand et al., 1987). We have investigated the first suite of eclogite and pyroxenite xenoliths from the recently discovered Voyageur kimberlite that is located within the northern portion of the Slave craton. Previous investigations of the northern Slave CLM focused on eclogites from the nearby Jericho kimberlite (De Stefano et al., 2009; Heaman et al., 2002, 2006; Kopylova et al., 1999a; Schmidberger et al., 2005; Smart et al., 2009, 2011, 2012, 2014), which forms part of the same kimberlite field as Voyageur, and revealed a compositionally diverse suite of eclogite xenoliths that, in addition to the predominant Paleoproterozoic eclogite ages, also bear a record of Mesoproterozoic overprinting of the CLM. Our study aims to further evaluate the impact of post-cratonisation tectonics on the highly diamondiferous Slave CLM (Helmstaedt, 2009). We discuss the major- and trace element compositions of garnet and clinopyroxene from the Voyageur eclogite and pyroxenite mantle-derived xenoliths, complemented with garnet oxygen isotope compositions, clinopyroxene Pb isotope compositions, and garnet $Fe^{3+}/\Sigma Fe$ contents. Our intent is to constrain whether the mafic component of the northern Slave CLM is related to subduction-driven imbrication of oceanic lithosphere during the Paleoproterozoic (as has been proposed for some Jericho eclogites), and to better understand CLM modification by younger tectonomagmatic events.

2. Regional geology

The Slave craton, located in northwest Canada (Fig. 1), is made up of an ancient (4.03–2.85 Ga) basement complex in the central and western portions of the craton and a juvenile, 2.72–2.55 Ga volcanic and granitoid terrain in the east (Bleeker and Hall, 2007). The western and eastern blocks were amalgamated at ca. 2.7–2.6 Ga, followed by widespread intrusion of 2.60–2.58 Ga granites (Bleeker et al., 1999; Davis et al., 2003). The Slave craton was modified along its southern and eastern margins in the Paleoproterozoic by the Taltson-Thelon orogeny, and along its western margin by the Wopmay Orogen (Hoffmann, 1989). Subduction of oceanic crust beneath the craton accompanied the ca. 1.9 Ga Wopmay orogeny, which is hypothesized to be responsible for extensive eclogite and diamond formation in the cratonic mantle (Aulbach et al., 2009a, 2009b; Heaman et al., 2002; Schmidberger et al., 2005, 2007; Smart et al., 2014). Additionally, this paleo-subduction zone has been geophysically imaged dipping eastward below the craton (Cook et al., 1999). The Slave craton was intruded by abundant mafic dykes between 2.2 and 1.8 Ga (Buchan et al., 2009), at 1.27 Ga during the event that formed the Mackenzie Large Igneous Province (LIP) with a focal point on the northwest of the craton (LeCheminant and Heaman, 1989), and again at ca. 720 Ma during the Franklin LIP event (Heaman et al., 1992). The Slave craton contains numerous kimberlite occurrences; Cretaceous to Eocene-aged kimberlites of the Lac de Gras field are found in the central Slave craton, compared to older Neoproterozoic and Jurassic kimberlite fields in the north and Ordovician and Cambrian occurrences in the south of the craton (Creaser et al., 2004; Heaman et al., 2003).

The Slave CLM is interpreted to be compositionally vertically and horizontally stratified (e.g. Griffin et al., 1999). Garnet xenocryst CaO-Cr_2O_3 compositions were used by Grütter et al. (1999) to divide the CLM into NE-trending northern, central and southern domains. The Voyageur kimberlite has a Jurassic age of 174 ± 10 Ma (U-Pb perovskite; S. Tappe, unpublished data), and occurs approximately 20 km west of the similarly aged Jericho (173 ± 1.3 Ma; Heaman et al., 2006) and Muskox kimberlites in the northern Slave domain (Fig. 1). Eclogite xenoliths have been extensively studied from the Jericho kimberlite. The abundant and diverse northern Slave mafic mantle component notably contains a high-MgO diamond-bearing eclogite suite, a high-FeO zircon-bearing suite, and barren, kyanite-bearing and bimineralic eclogite types (Heaman et al., 2002; Kopylova et al., 1999a; Smart et al., 2009; De Stefano et al., 2009). Previous studies of the Jericho eclogites indicate Paleoproterozoic protolith formation within oceanic lithosphere (Heaman et al., 2002, 2006; Schmidberger et al., 2005; Smart et al., 2012, 2014), with subsequent oxidizing metasomatism that produced diamonds in some eclogite types (Smart et al., 2009, 2011). In contrast to the central and southern Slave craton domains that contain a shallow ultra-depleted harzburgitic and dunitic layer, the northern domain contains abundant eclogite and fertile lherzolites in the deeper cratonic mantle lithosphere that bear a significant metasomatic signature (Griffin et al., 2004; Kopylova and Russell, 2000).

3. Analytical methods

3.1. Major- and minor element concentrations

Major- and minor elements were analyzed in garnet and clinopyroxene (± phlogopite and rutile) using a JEOL 8900 electron microprobe at the University of Alberta. A 20 nA beam current and 20 kV accelerating voltage were used. Multiple grains of garnet and clinopyroxene were analyzed for each xenolith, with a minimum of 5 analyses per mineral grain and care was taken to analyze adjacent garnet and clinopyroxene mineral pairs.

3.2. Trace element concentrations

Trace element contents of garnet and clinopyroxene were obtained using laser ablation inductively coupled plasma mass spectrometry (LA-ICP-MS) at the Central Analytical Facility of Stellenbosch University, South Africa. Between 3 and 8 grains of garnet and clinopyroxene were

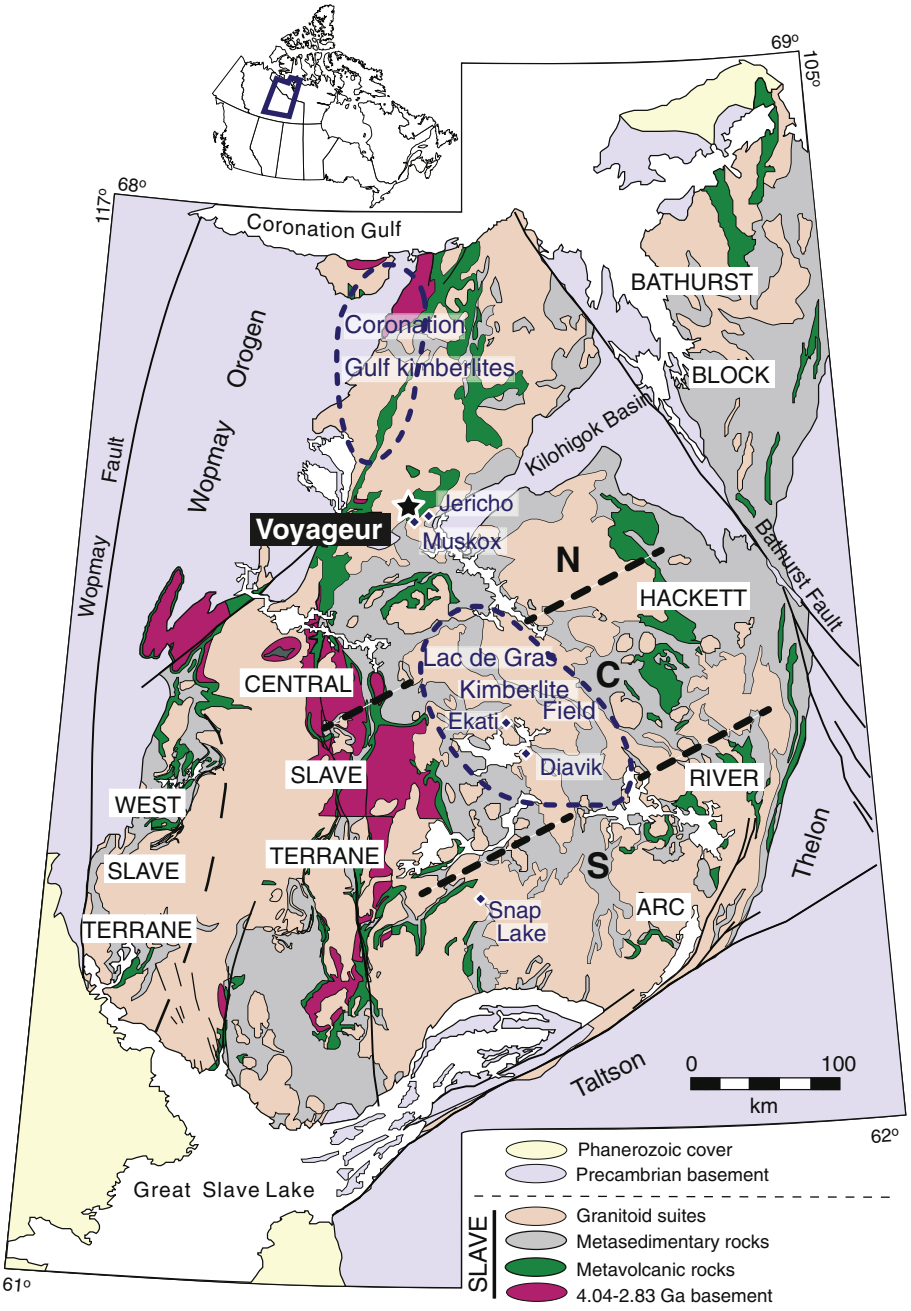

Fig. 1. Map displaying the general geology of the Slave craton, located in northwestern Canada.
Modified from Tappe et al. (2013). The Slave craton lithospheric mantle has been divided into the Northern (N), Central (C) and Southern (S) domains, based on xenocrystic garnet compositions by Grütter et al. (1999). The Voyageur kimberlite (black star) is found in the Northern domain, located approximately 150 km north of the central Slave Lac de Gras kimberlite field, and 20 km west of the Jericho kimberlite occurrence.

analyzed in each xenolith. The LA-ICP-MS system includes a 193 nm excimer laser system coupled to an Agilent 7500ce quadrupole ICP-MS. Internal standardization used ^{29}Si, and NIST SRM 610 standard reference glass (Pearce et al., 1997) was the external calibration standard. A beam diameter of 100 μm was used and backgrounds were measured for 20 s followed by ablation time of 20 s. Reduction of time-resolved data and concentration calculations were performed off-line using the GLITTER software package (Van Achterbergh et al., 2001). Analyses of the NIST SRM 612 and BCR standard reference glasses were performed with every ten unknowns. The standard results are consistently within 2σ of the average concentrations reported by Pearce et al. (1997) and have standard errors between 2 and 6%, relative (see Appendix A). The minimum detection limit for most of the elements quantified is <0.2 ppm.

3.3. Oxygen isotope analysis of garnet

The oxygen isotope composition of fresh, inclusion- and crack-free garnet from mineral separates of selected Voyageur eclogites was determined by laser fluorination at the University of Cape Town, South Africa using the methods described by Harris and Vogeli (2010). All oxygen isotope ratios were measured offline using a Finnigan Delta XP mass spectrometer in dual-inlet mode, and yields were determined by measuring the gas pressure in the mass spectrometer inlet at a constant

volume, which was in all cases close to 100% (based on the weight of the sample). Our data were normalized to two splits (for each 10 unknown analyses) of the internal standard MON GT, which has a $\delta^{18}O$ value of 5.38‰ (Harris and Vogeli, 2010) and yielded a 2-sigma standard deviation of 0.16‰ for our analytical sessions. The long-term reproducibility of MON GT is better than 0.13‰ (2σ; n = 179). San Carlos olivine grains were also measured using the same method, and yielded an average $\delta^{18}O$ value of 5.33‰ (±0.32‰, 2σ; n = 9), which is within error of the accepted value of 5.35‰ (Eiler et al., 2011).

3.4. In-situ Pb isotope analysis of clinopyroxene

The Pb isotope compositions of individual clinopyroxene mineral separates obtained from selected Voyageur eclogites were determined at the MITERAC ICP-MS Facility, University of Notre Dame (USA). Inclusion and crack-free crystals were targeted to avoid kimberlite contamination (see below). In situ Pb isotope ratios were measured utilizing a NWR193 nm laser ablation system coupled to a Nu Plasma II MC-ICP-MS instrument. Individual clinopyroxene grains were rastered using a 150 μm spot size, between 7 and 12 Hz repetition rate, and an energy density of 10–12 J/cm^3. Individual analyses consisted of 45 s on peak blank measurement followed by a 60 s laser ablation interval, and raw data were reduced using the Nu Instruments TRA (Time-Resolved-Analysis) software. Six grains from each of the samples were analyzed and the unknown analyses were bracketed by analysis (n = 4 measurements) of the NIST SRM 614 glass standard in order to correct for instrumental drift and mass bias. As described in Chen and Simonetti (2015), the instrumental mass bias was corrected by adopting the exponential law and the Pb isotope values for NIST SRM 614 reported in Baker et al., 2004. Based on the repeated measurements (n = 32) of the NIST SRM 614 standard, the average external reproducibility (2σ level) for the $^{208}Pb/^{204}Pb$, $^{207}Pb/^{204}Pb$, $^{206}Pb/^{204}Pb$, $^{207}Pb/^{206}Pb$, and $^{208}Pb/^{206}Pb$ ratios are ±0.14, 0.059, 0.066, 0.0015, and 0.003, respectively.

In addition, a typical fresh hypabyssal magmatic kimberlite sample from Voyageur was analyzed for its Pb isotope composition (Table 5). The bulk kimberlite powder was processed through standard acid digestion procedures and Pb was separated using anion exchange resin Bio-Rad AG1-X8 applying a HCl-HBr technique (as outlined in Tappe et al., 2017, 2016). The kimberlite Pb isotopic compositions were measured on a Finnigan MAT 262 instrument on single Re filaments in static mode (GFZ Potsdam, Germany). Instrumental fractionation was corrected with 0.1% per a.m.u. as determined from the long-term reproducibility of Pb reference material NBS-981. Accuracy and precision of the reported Pb isotope ratios are better than 0.1% at the 2σ level of uncertainty.

3.5. Garnet $Fe^{3+}/\Sigma Fe$ contents

The Fe^{3+} contents, reported in Table 1 in terms of $Fe^{3+}/\Sigma Fe$, were determined by Mössbauer spectroscopy at Goethe Universität Frankfurt, Germany. All spectra were obtained at room temperature in constant acceleration mode with a velocity ramp of ±5 mm s^{-1} and a ~ 50 mCi ^{57}Co in Rh source. Mirror-image spectra were collected over 512 channels until ~3 × 10^6 counts per channel were reached. The spectra were calibrated with respect to α-Fe metal. Optically clean, inclusion and crack-free garnet mineral separates of selected Voyageur xenoliths were ground under acetone and mixed with a small quantity of sugar prior to packing into a hole drilled into a 1 mm thick Pb disc that served as a sample holder by closing off with tape. The amount of garnet (generally ~2–5 mg) and sample diameter were adjusted to produce sample thicknesses <5 mg cm^{-2} in order to minimize saturation effects. Fitting of folded spectra followed the approach described by Woodland and Koch (2003), including a correction to account for differing recoil free fractions of Fe^{3+} and Fe^{2+} in garnet (Woodland and Ross, 1994). In only three cases was it necessary to constrain the Fe^{3+}-peak width to 0.4 mm s^{-1} in order to obtain meaningful hyperfine parameters. Corrected $Fe^{3+}/\Sigma Fe$ values are reported in Table 1 and have absolute uncertainties of ±0.01.

4. Samples and petrography

A suite of twenty-two xenoliths from the Voyageur kimberlite has been investigated, including 19 eclogites and 3 pyroxenites. Xenoliths were recovered from large diameter drill core into the hypabyssal kimberlite body. A summary of xenolith mineralogy is provided in Table 1. The pyroxenites were distinguished from the eclogites by clinopyroxene with low Na_2O contents and high modal abundances (>75 vol%). The eclogites are composed of roughly equal amounts of orange-red to pink garnet and bright to dark green clinopyroxene; minor (<1%) rutile, phlogopite, orthopyroxene, and apatite are also observed in some samples. The Voyageur xenoliths appear variably fresh, and most samples were affected by only minor alteration, kimberlite infiltration, and garnet kelyphitization. In samples where alteration or mineral inclusions were present, only clear portions of garnet and clinopyroxene grains were used for in-situ trace element and isotopic analyses. Eclogites #361, 346, 378, 344, 374, 376, 395 show a greater degree of alteration, cloudy clinopyroxene, and the presence of small secondary veins consisting of fine-grained material and carbonate. There appears to be at least two textural groupings; one group (e.g. xenoliths #346, 362A, 362B, 380A, 390; see Fig. 2a, b) is medium- to coarse-grained, with equigranular textures – equivalent to the massive texture of Kopylova et al. (1999a) – and light orange-pink garnet and pale green clinopyroxene. The second group (e.g. xenoliths #370, 378, 380B, 386A, 408; see Fig. 2c, d) displays foliated textures – equivalent to the anisotropic and foliated textures of Kopylova et al. (1999a) – where the garnet and clinopyroxene grains appear to be slightly elongated and aligned, and garnet is orange-red and clinopyroxene is a bright to dark green. The pyroxenite xenoliths (e.g. #383A, 383B, 393; see Fig. 2e, f) contain garnet and clinopyroxene of a similar colour to the foliated eclogite group, but do not have foliated textures and contain significantly more clinopyroxene (>75 vol%); 5 vol% of orthopyroxene is also found in xenolith #393. Eclogite xenolith #390 displays a unique layered texture composed of discrete bands of massive-textured clinopyroxene and garnet with significant coarse-grained phlogopite.

5. Results

5.1. Major element mineral compositions

The major- and minor element contents of minerals from the Voyageur xenoliths are listed in Table 1. The Voyageur eclogites and pyroxenites all contain low-Cr garnets with <0.08 wt.% Cr_2O_3; garnet from the pyroxenite #393 (an orthopyroxene-bearing xenolith) contains 0.25 wt.% Cr_2O_3. Garnet has variable MgO (4.77–12.3 wt.%), FeO (15.0–27. 5 wt.%) and CaO (3.61–15.6 wt.%) contents, with Mg-numbers ranging from 26 to 58. The pyrope-almandine-grossular garnet compositions are displayed on Fig. 3a, and all garnets from the Voyageur xenoliths geochemically classify as Group B or C (Coleman et al., 1965). Garnets with "high-MgO" compositions (>18 wt.% MgO) are absent in the Voyageur xenoliths, in contrast to the nearby Jericho kimberlite that contains abundant high-MgO garnet composition in eclogites (Heaman et al., 2006; Smart et al., 2009; De Stefano et al., 2009). Garnet from the three Voyageur pyroxenites have high FeO contents (23.1–24.3 wt.%) and the lowest CaO contents (4.0–4.9 wt.%) of all studied Voyageur xenoliths.

Clinopyroxene from the Voyageur eclogites have a wide range of compositions, and classify as Group B and C using the MgO vs. Na_2O diagram from (Taylor and Neal, 1989) (Fig. 3b), excluding clinopyroxene from the pyroxenites that plot in the Group A field. Group C clinopyroxene have higher Na_2O (6.8–9.0 vs. 4.4–6.7 wt.%; Fig. 3ab) and Al_2O_3 (10.5–18.2 vs. 5.2–13.0 wt.%) contents than the Group B clinopyroxene (e.g. jadeite components of 27–57 vs. 39–52 mol%), but

Table 1
Major and minor element composition of garnet and clinopyroxene from the Voyageur xenoliths.

	346	362A	362B	380A	390	361	370	378	380B	386A	408	395	352
Mineralogy	gt + cpx	gt + cpx	gt + cpx	gt + cpx	gt + cpx	gt + cpx	gt + cpx	gt + cpx	gt + cpx	gt + cpx	gt + cpx	gt + cpx	gt + cpx
Minor phases				ap	phl								
Trace phases	phl	ap	ap, rt			ap, rt	rt	ilm, ap	rt	rt	rt	rt	ilm,
Comment	Mild alt				layered	altered						altered	altered
	Gt	Gt	Gt	Gt	Gt	Gt	Gt	Gt	Gt	Gt	Gt	Gt	Gt
SiO_2	39.99	40.73	40.34	39.73	39.73	39.66	39.96	39.31	39.92	38.74	39.51	39.10	38.54
TiO_2	0.12	0.09	0.07	0.18	0.06	0.28	0.13	0.15	0.24	0.15	0.11	0.12	0.19
Al_2O_3	22.46	23.01	22.77	22.40	22.44	22.10	22.28	21.93	22.07	20.88	21.94	21.89	21.48
Cr_2O_3	0.01	0.04	0.08	0.01	0.03	0.02	0.04	0.02	0.01	0.02	0.04	0.01	0.01
FeO	18.83	14.95	21.22	19.28	19.35	17.76	20.60	24.61	15.49	27.52	22.73	23.77	21.49
MnO	0.27	0.30	0.41	0.37	0.32	0.55	0.36	0.41	0.72	0.51	0.45	0.48	0.36
MgO	10.80	11.60	12.26	6.74	10.74	7.42	8.44	5.88	7.66	5.44	7.30	7.35	4.95
CaO	7.36	9.64	3.61	12.04	6.95	12.37	9.06	8.85	13.82	7.31	8.54	7.68	12.58
Na_2O	0.07	0.05	0.05	0.10	0.05	0.13	0.06	0.07	0.11	0.06	0.05	0.06	0.10
K_2O	0.00	0.00	0.00	0.00	0.00	0.01	0.00	0.00	0.00	0.00	0.00	0.00	0.01
Total	99.9	100.4	100.8	100.86	99.7	100.29	100.94	101.2	100.0	100.6	100.7	100.5	99.70
Mg#	0.51	0.58	0.51	0.38	0.50	0.43	0.42	0.30	0.47	0.26	0.36	0.36	0.29
$Fe^{3+}/\sum Fe^*$	0.026	0.027	0.022	0.023		0.039	0.037	0.029			0.036	0.041	
Rock Class.	Eclogite	Eclogite	Eclogite	Eclogite	Eclogite	Eclogite	Eclogite	Eclogite	Eclogite	Eclogite	Eclogite	Eclogite	Eclogite
Garnet Class.	B	B	B	C	B	C	B	C	B/C	C	C	C	C
Trace Ele Class.	Gabbroic	Gabbroic	Gabbroic	Gabbroic	Gabbroic	Basaltic	Basaltic	Basaltic	Basaltic	Basaltic	Basaltic	N/a	N/a

	346	362A	362B	380A	390	361	370	378	380B	386A	408	395	352
	Cpx	Cpx	Cpx	Cpx	Cpx	Cpx	Cpx	Cpx	Cpx	Cpx	Cpx	Cpx	Cpx
SiO_2	55.43	56.31	55.60	55.95	55.49	55.36	55.95	55.89	54.75	53.66	55.00	54.33	55.84
TiO_2	0.20	0.19	0.17	0.38	0.14	0.44	0.16	0.20	0.31	0.21	0.13	0.14	0.36
Al_2O_3	8.90	13.03	6.33	13.45	10.07	12.10	9.12	10.53	9.24	5.15	6.75	5.72	15.33
Cr_2O_3	0.01	0.07	0.09	0.02	0.03	0.03	0.05	0.02	0.02	0.03	0.04	0.01	0.01
FeO	4.48	2.07	5.88	4.76	3.61	4.93	4.74	6.27	4.84	10.07	6.52	7.47	4.52
MnO	0.03	0.02	0.07	0.03	0.04	0.03	0.04	0.04	0.05	0.07	0.05	0.05	0.03
MgO	10.11	8.42	11.65	6.59	9.60	7.45	9.79	7.77	9.49	9.81	10.47	10.53	5.66
CaO	14.72	12.99	15.40	10.33	14.00	11.50	14.82	12.69	14.60	16.04	16.31	16.52	8.82
Na_2O	5.84	6.70	4.68	8.55	6.20	7.94	5.51	6.78	6.01	4.40	4.52	4.39	8.98
K_2O	0.02	0.02	0.02	0.01	0.02	0.01	0.02	0.01	0.01	0.02	0.01	0.02	0.01
Total	99.74	99.82	99.89	100.07	99.19	99.78	100.20	100.19	99.31	99.45	99.80	99.20	99.54
Mg#	0.80	0.88	0.78	0.71	0.83	0.73	0.79	0.69	0.78	0.63	0.74	0.72	0.69

	376	342	344	392	409	374	383A	383B	393
Mineralogy	gt + cpx	gt + cpx	gt + cpx	gt + cpx	gt + cpx	gt + cpx	gt + cpx	gt + cpx	gt + cpx
Minor phases									opx
Trace phases	ilm	ol, phl	rt						ol
Comment	alt.		alt. infil.			alt. infil.			
	Gt	Gt	Gt	Gt	Gt	Gt	Gt	Gt	Gt
SiO_2	38.98	39.09	39.69	38.94	38.78	38.91	40.00	38.99	39.57
TiO_2	0.17	0.13	0.07	0.13	0.31	0.08	0.09	0.10	0.11
Al_2O_3	21.61	21.87	22.22	21.78	21.23	21.41	22.19	21.70	21.14
Cr_2O_3	0.01	0.04	0.06	0.02	0.01	0.03	0.08	0.08	0.25
FeO	18.14	20.64	17.10	20.06	22.07	23.70	23.10	23.30	24.30
MnO	0.26	0.35	0.37	0.29	0.59	0.56	0.54	0.55	0.64
MgO	4.77	8.08	10.46	6.92	5.53	6.96	10.81	10.72	9.61
CaO	15.57	9.65	9.38	11.49	11.49	8.40	3.97	4.01	4.88
Na_2O	0.05	0.06	0.04	0.05	0.13	0.04	0.04	0.04	0.03
K_2O	0.00	0.01	0.01	0.01	0.01	0.00	0.00	0.00	0.00
Total	99.59	99.91	99.40	99.68	100.1	100.1	100.8	99.5	100.5
Mg#	0.32	0.41	0.52	0.38	0.31	0.34	0.45	0.45	0.41
$Fe^{3+}/\sum Fe^*$	0.030						0.043		
Rock Class.	Eclogite	Eclogite	Eclogite	Eclogite	Eclogite	Eclogite	Pyroxenite	Pyroxenite	Pyroxenite
Grt Class	C	B/C	B	C	C	C	B	B	B
TE Class.	N/a	N/a	N/a	N/a	N/a	N/a	Pyrox.	Pyrox.	Pyrox.

	376	342	344	392	409	374	383A	383B	393	393
	Cpx	Cpx	Cpx	Cpx	Cpx	Cpx	Cpx	Cpx	Cpx	Opx
SiO_2	57.17	55.99	55.81	56.72	55.90	55.59	54.76	53.86	54.14	55.06
TiO_2	0.17	0.15	0.14	0.16	0.25	0.16	0.09	0.09	0.05	0.02
Al_2O_3	18.15	10.12	11.39	16.31	11.85	10.19	3.06	2.97	1.30	0.30
Cr_2O_3	0.01	0.05	0.08	0.01	0.01	0.04	0.04	0.06	0.08	0.01

Table 1 (*continued*)

	376	342	344	392	409	374	383A	383B	393	393
	Cpx	Cpx	Cpx	Cpx	Cpx	Cpx	Cpx	Cpx	Cpx	Opx
FeO	2.94	4.80	3.30	3.15	5.74	5.93	7.66	7.78	7.85	18.82
MnO	0.01	0.03	0.02	0.02	0.03	0.04	0.11	0.11	0.11	0.20
MgO	4.75	9.30	9.25	5.71	7.48	8.39	13.54	13.76	14.52	26.39
CaO	8.70	14.04	13.63	9.39	11.74	12.65	17.96	18.05	20.25	0.40
Na_2O	8.63	5.59	5.90	8.22	7.19	6.51	2.50	2.55	1.50	0.06
K_2O	0.02	0.01	0.01	0.01	0.01	0.01	0.01	0.01	0.02	0.00
Total	100.53	100.08	99.54	99.69	100.21	99.51	99.73	99.23	99.79	101.26
Mg#	0.74	0.78	0.83	0.76	0.70	0.72	0.76	0.76	0.77	0.71

Mg# explained in text; bd = below detection; * determined by Mössbauer spectroscopy.
Gt = garnet; cpx = clinopyroxene; opx = orthopyroxene; ol = olivine; ap = apatite; rt = rutile; ilm = ilmenite; phl = phlogopite; alt = altered; infil = infiltrated.
Garnet classification discussed in Section 5.1 and Fig. 3. Trace element classification discussed in Section 6.2 and Fig. 9.
Major element contents in wt.%.

also have lower CaO and MgO contents (8.7–12.7 vs. 12.7–16.5 and 4.8–7.8 vs. 8.4–11.7 wt.%, respectively; e.g. diopside component). Clinopyroxene from the three pyroxenites have the lowest Na_2O (1.5–2.6 wt.%) and Al_2O_3 (1.3–3.1 wt.%) contents (e.g. jadeite components of 8–16 mol%), and the highest CaO and MgO (18.0–20.3 wt.% and 13.5–14.5 wt.%, respectively) contents. Pyroxenite #393 also contains orthopyroxene, which is characterized by 18.8 wt.% FeO, 26.4 wt.% MgO, 0.3 wt.% Al_2O_3 and a Mg-number of 71.

5.2. Trace element mineral compositions

Thirteen of the Voyageur eclogites were analyzed for trace element contents based on sample size and alteration, and the results are listed in Table 2. Garnet from the Voyageur eclogites and pyroxenites have Ni contents between 1.5 and 21 ppm, compared to the average of ~40 ppm for eclogitic garnet worldwide (Jacob, 2004). Garnet from the Voyageur pyroxenites has high V (420–473 ppm), Sc (120–135 ppm), and Y (50–84 ppm) compared to Voyageur eclogitic garnet (average 126 ppm V, 54 ppm Sc, and 37 ppm Y). Most garnet has very low Ba contents (<0.2 ppm), but those with elevated Ba (up to 1.3 ppm) variably show enrichments in the LREE and other incompatible elements. The chondrite-normalized Rare Earth Element (REE) patterns of Voyageur eclogitic garnet (Fig. 4a) are similar to those commonly observed in eclogitic garnet worldwide (e.g. Jacob, 2004), and the nearby Jericho kimberlite (Smart et al., 2014). Garnet displays either flat or slightly depleted Heavy REEs (HREEs) with Lu_N/Gd_N values (subscript N indicates chondrite-normalization with values from McDonough and Sun, 1995) of 0.3–1.4 and Lu_N values between 7 and 47. Garnet from the pyroxenites #383A and #393 display more fractionated HREE patterns (Lu_N/Gd_N = 1.5–2.9). The Voyageur eclogitic garnets display small Eu

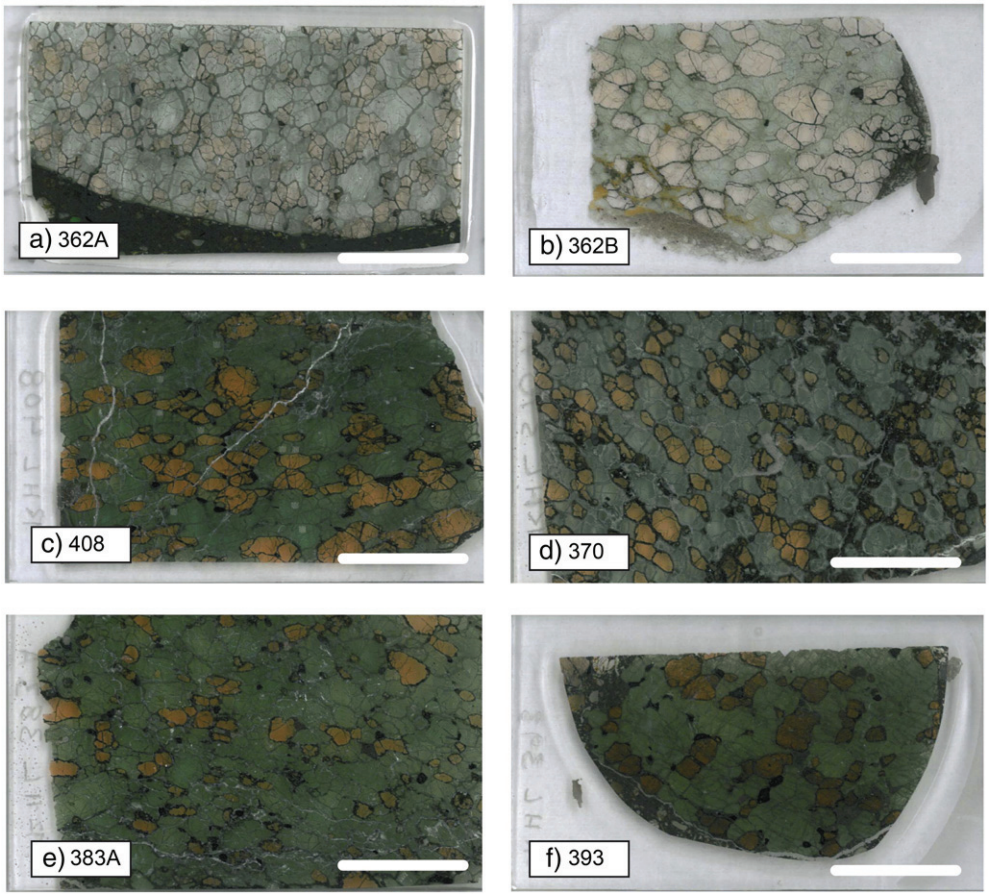

Fig. 2. Select Voyageur xenoliths. Eclogites: (a) 362A (b) 362B (c) 408 and (d) 386A. Pyroxenites: (e) 383A and (f) 393. Scale bar is 10 mm.

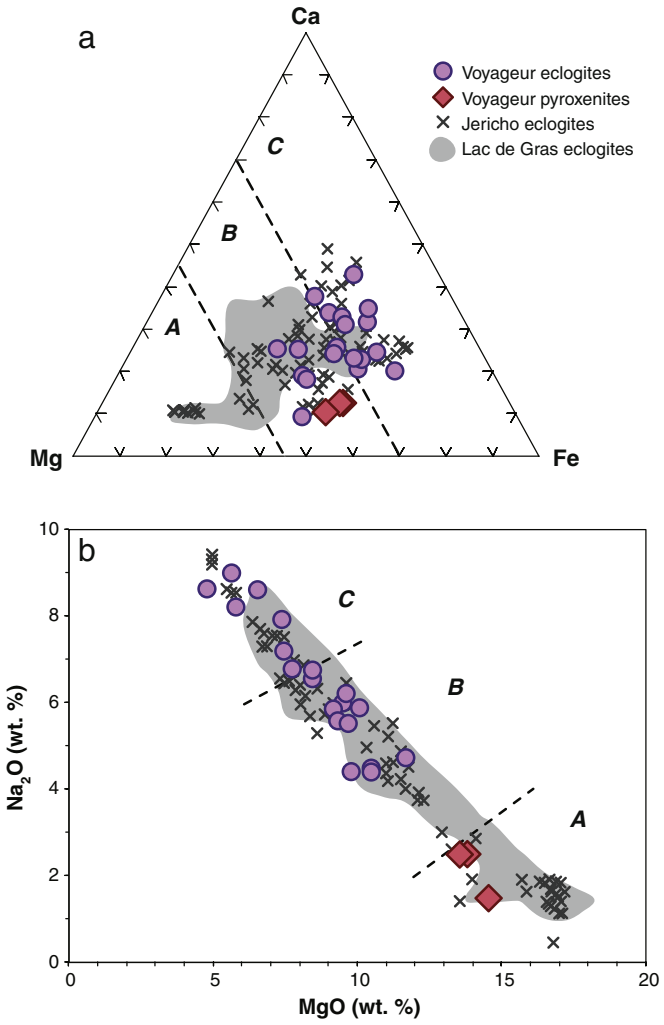

Fig. 3. (a) Molar Ca-Mg-Fe composition of garnets from the Voyageur xenoliths. Garnets from northern Slave Jericho and Muskox eclogite xenoliths from Heaman et al. (2006), Kopylova et al. (1999a), and Smart et al. (2009, 2014). Garnets from central Slave Lac de Gras eclogite xenoliths (shaded field) from Aulbach et al. (2007), and Schmidberger et al. (2007). A-B-C classification scheme from (Coleman et al., 1965). (b) Na_2O vs. MgO contents of clinopyroxene from Voyageur xenoliths. A-B-C classification from Taylor and Neal (1989). Data sources and symbols as in (a).

anomalies (calculated as $2 * Eu_N / [Sm_N + Gd_N]$) of 1.1–1.5; pyroxenitic garnet have less distinct Eu anomalies of 0.8–1.1.

The Voyageur eclogites contain clinopyroxene with normalized REE patterns that display relative depletions in La to Ce (La_N between 0.8 and 11; excluding sample #361 with $La_N = 66$), flat MREEs and depletion in the HREEs (Fig. 4b). Eu anomalies are absent or weak in the Voyageur clinopyroxene ($Eu^* = 1.0–1.2$). The Voyageur eclogitic clinopyroxene contain between 35 and 824 ppm Sr, 0.1 and 21.5 ppm Pb and below detection limits of U and Th (excluding the altered sample *361*). Clinopyroxene from Voyageur pyroxenites #383A and #393 have 995 and 202 ppm Sr, 13.3 and 1.4 ppm Pb, respectively. The Voyageur eclogite clinopyroxene have positive Sr anomalies (calculated as primitive-mantle normalized $2 * Sr / [Pr + Nd]$) between 2 and 11.3, excluding the altered eclogite #361 which has a Sr^* of 0.4, and clinopyroxene from the Voyageur pyroxenite have absent or lower Sr^* of 0.9 and 1.9.

5.3. Thermobarometry

Equilibration temperatures and pressures were calculated using two methods (Table 3). Eclogite pressure-temperature equilibration conditions were iteratively calculated using the thermometer of Ellis and Green (1979), T_{EG79}, in combination with pressure estimates from the Voyageur peridotite-defined geotherm, P_{V06}, which was constrained by Verigeanu (2006) using the single clinopyroxene barometer and thermometer of Nimis and Taylor (2000), T_{NT2000}. The $T_{EG79} - P_{V06}$ calculations yielded conditions between 902 and 1233 °C and 43–68 kbar for the eclogites, and between 846 and 914 °C and 39–44 kbar for the pyroxenites. Temperatures calculated for the pyroxenites at 4 GPa using T_{NT2000} were between 920 and 970 °C, and the 2-pyroxene thermometer of Taylor (1998), T_{TA98}, was applied to pyroxenite #393, yielding a temperature of 940 °C (Table 3). These different thermometers (T_{EG79}, T_{NT00} and T_{TA98}) yielded results within 40–60 °C of each other.

The second method involves iterative calculations of T_{EG79} and pressure using the barometer of Beyer et al. (2015), P_{B15}, for eclogites that contain clinopyroxene with [Si] < 1.995 per formula unit. Therefore, this method cannot be applied to eclogites #362B, 370, 378, 395 and 408 and pyroxenites #383A and #393. The calculated uncertainties using the Beyer expression for the remaining eclogites are between 10 and 13%. The $T_{EG79} - P_{B15}$ calculations yielded conditions of 873–1198 °C and 34–59 kbar for the eclogites. Pyroxenite #383B yielded $T_{EG79} - P_{B15}$ of 873 °C and 34 kbar. The %-difference between the two PT methods is <4% for temperature, but up to 25% for pressure. For this reason, the results of both thermobarometric techniques are presented in Fig. 5, and the $T_{EG79} - P_{V06}$ calculation is used in the following discussion and oxybarometry calculations.

5.4. Garnet ferric iron contents and eclogite oxybarometry

The $Fe^{3+}/\Sigma Fe$ values for garnet from selected Voyageur eclogites (n = 10) are reported in Table 1, and range between 0.021 and 0.041 (±0.01); garnet from the Voyageur pyroxenite #383A has a $Fe^{3+}/\Sigma Fe$ of 0.043 ± 0.01. The Voyageur garnets have a smaller range of $Fe^{3+}/\Sigma Fe$ values compared to garnets from eclogites of the nearby Jericho and Muskox kimberlites (0.019–0.076, n = 13; Kopylova et al., 2016) and worldwide eclogitic garnets (0.02–0.09, n = 10; excluding an anomalous value of 0.16; data compiled by Stagno et al., 2015). The $\Delta \log fO_2$ values (relative to the FMQ buffer) were calculated using the equilibration of Stagno et al. (2015), applying our T_{EG79} and P_{V06} estimates (Table 3) as intensive variable input parameters. The eclogites have $\Delta \log fO_2$ values ranging between FMQ-1.5 and FMQ-4.6, and the pyroxenite has a value of FMQ-3.2 (Fig. 6). Uncertainties associated with the oxybarometric calculations are ±0.5 log units.

5.5. Garnet oxygen isotope composition

Garnet from the Voyageur xenoliths (Table 4) have $\delta^{18}O$ values between 5.2 and 6.2‰, with an average of 5.7 ± 0.3‰ ($1\sigma = 18$). Garnets from Voyageur pyroxenites have $\delta^{18}O$ values between 5.6 and 5.9‰, (n = 3).

5.6. Clinopyroxene Pb isotope compositions

The Pb isotope compositions were determined for clinopyroxene from 7 eclogites and one pyroxenite, and average isotope ratios are reported in Table 5 (the full dataset can be found in Appendix B). Voyageur eclogitic clinopyroxenes have a range of $^{206}Pb/^{204}Pb$ from 14.9–20.7 and $^{207}Pb/^{204}Pb$ from 15.1–17.1, whereas clinopyroxene from the pyroxenite #383A has average isotopic compositions of 15.6 ± 0.2 (2 standard deviations) and 15.3 ± 0.06, respectively. The host 174 ± 10 Ma Voyageur hypabyssal kimberlite has $^{206}Pb/^{204}Pb_{174\ Ma}$ of 18.78 and $^{207}Pb/^{204}Pb_{174\ Ma}$ of 15.61 (Table 5). The xenolith clinopyroxene Pb isotope data have not been corrected for isotopic ingrowth because parent-daughter element ratios were not measured. The measured isotope ratios are assumed to approximate the initial isotope values, given the very low U concentrations (below 0.1 ppm) and calculated low U/Pb ratios (0.002–0.03) of the Voyageur clinopyroxene (Table 2).

Table 2
Trace element compositions of garnet and clinopyroxene from Voyageur xenoliths.

	346	362A	362B	380A	390	361	370	378	380B	386A	408	383A	393
TE Class	Gabb.	Gabb.	Gabb.	Gabb.	Gabb.	Metasom. Bas.	Bas.	Bas.	Bas.	Bas.	Bas.	Pyrox.	Pyrox.
	Gt	Gt	Gt	Gt	Gt	Gt	Gt	Gt	Gt	Gt	Gt	Gt	Gt
V	44	76	106	49	444	87	142	179	122	268	238	235	73
Ni	21	14	6.4	4.2	9.8	8.1	7.5	3.7	1.5	2.6	8.4	11	13
Sc	27	61	49	24	135	61	56	53	94	61	76	120	37
Rb	0.02	0.43	0.11	0.01	0.03	0.06	0.04	0.01	0.01	0.01	0.01	0.01	0.01
Ba	0.28	0.55	0.35	0.12	0.83	0.11	b.d.	0.07	b.d.	0.03	0.05	0.18	0.15
Th	0.01	0.03	0.004	0.004	0.03	0.01	0.004	b.d.	0.01	b.d.	0.005	0.01	0.01
U	0.01	0.04	0.003	0.01	0.01	0.01	b.d.	0.005	0.02	0.01	0.01	0.01	0.004
Nb	0.04	0.02	0.01	0.03	0.04	0.22	0.004	b.d.	0.25	b.d.	0.01	0.02	0.05
Ta	0.003	0.01	0.003	0.003	0.01	0.01	0.005	0.003	0.03	0.003	0.003	0.005	0.006
La	0.02	0.07	0.03	0.01	0.09	0.06	0.01	0.01	0.02	0.01	0.01	0.01	0.01
Ce	0.22	0.30	0.15	0.25	0.20	0.35	0.12	0.15	0.30	0.12	0.16	0.24	0.21
Pr	0.09	0.16	0.06	0.12	0.08	0.15	0.08	0.08	0.13	0.08	0.1	0.13	0.11
Pb	0.14	1.1	0.19	0.03	0.03	0.09	b.d.	0.06	0.07	b.d.	0.05	0.77	0.17
Sr	0.43	2.4	0.51	1.18	0.36	0.77	1.29	0.94	0.44	0.68	0.84	0.50	1.0
Nd	1.3	2.4	0.75	2.0	1.3	1.8	1.6	1.5	2.0	1.3	1.7	1.7	1.9
Sm	1.5	2.7	1.1	2.3	2.4	2.4	2.1	2.6	2.1	2.4	2.7	1.5	2.2
Zr	8.3	11	9.7	17	19	39	9.4	12	68	7.8	6.2	9.6	5.5
Hf	0.07	0.13	0.13	0.25	0.58	0.58	0.16	0.22	1.2	0.13	0.11	0.20	0.11
Eu	1.1	1.7	0.79	1.9	1.2	1.6	1.3	1.8	1.3	1.5	1.6	0.87	1.6
Ti	557	683	426	897	635	1485	766	888	1160	778	658	570	353
Gd	3.7	4.5	2.7	5.9	7.7	6.3	4.5	7.2	5.3	6.7	5.3	3.6	4.0
Tb	0.71	0.68	0.57	1.1	1.8	1.4	0.92	1.5	1.3	1.5	1.0	0.99	0.74
Dy	4.6	3.5	3.8	6.2	14	10	6.2	10	9.4	11	7.3	7.7	4.9
Y	22.9	15.2	20.7	29.9	83.8	53.3	32.9	54.2	50	63.6	40.4	49.7	25.5
Ho	0.97	0.63	0.86	1.2	3.4	2.2	1.4	2.2	2.2	2.6	1.6	2.1	1.1
Er	2.0	1.4	2.3	2.7	9.7	6.0	3.7	6.1	5.8	7.5	4.7	6.3	2.8
Tm	0.24	0.22	0.35	0.35	1.4	0.89	0.54	0.88	0.82	1.1	0.76	1.0	0.39
Yb	1.4	1.3	2.2	2.2	9.6	5.6	3.5	5.8	5.0	7.4	5.2	7.5	2.5
Lu	0.20	0.18	0.35	0.32	1.4	0.86	0.56	0.92	0.70	1.16	0.83	1.29	0.35
Eu*	1.3	1.5	1.3	1.5	0.8	1.2	1.3	1.2	1.1	1.1	1.3	1.1	1.6
Lu/Gd	0.4	0.3	1.1	0.4	1.5	1.1	1.0	1.0	1.1	1.4	1.3	2.9	1.4
	346	362A	362B	380A	390	361	370	378	380B	386A	408	383A	393
	Cpx	Cpx	Cpx	Cpx	Cpx	Cpx	Cpx	Cpx	Cpx	Cpx	Cpx	Cpx	Cpx
V	165	254	489	223	484	260	379	561	432	709	614	467	334
Ni	282	137	110	40	195	75	105	59	15	59	153	197	227
Sc	12	20	31	12	54	14	27	28	40	50	41	58	18
Rb	0.01	0.59	0.49	0.28	0.05	0.25	0.01	0.01	0.02	0.01	0.10	0.06	0.22
Ba	0.22	11	0.75	0.05	3.5	2.7	0.47	0.09	0.22	0.26	0.44	1.3	0.78
Th	0.01	0.06	0.04	0.004	0.07	0.67	0.01	0.02	0.02	0.02	0.02	0.10	0.02
U	0.01	0.01	0.07	0.003	0.01	0.15	b.d.	0.004	0.01	0.01	0.01	0.03	0.003
Nb	0.08	0.10	0.01	0.07	0.18	0.22	0.01	0.004	0.48	0.003	0.003	0.005	0.008
Ta	0.01	0.002	0.001	0.005	0.005	0.03	0.001	0.001	0.17	b.d.	0.001	0.001	0.001
La	1.1	0.42	2.8	0.20	2.0	16	0.23	0.39	0.53	1.1	1.2	7.7	1.9
Ce	4.5	2.5	14	0.88	12	35	1.5	1.9	2.1	4.9	3.8	37	6.7
Pr	0.85	0.68	2.8	0.17	2.5	4.6	0.41	0.44	0.38	1.1	0.82	7.1	1.4
Pb	0.44	1.9	2.2	0.07	1.4	0.19	3.6	0.47	21	1.1	1.7	13.3	4.0
Sr	182	544	824	35	202	126	448	268	63	398	752	995	588
Nd	4.7	4.7	16.8	1.1	15.6	20	3.0	3.1	2.1	6.5	5.4	32.3	8.6
Sm	1.2	1.2	3.9	0.35	4.8	3.3	0.80	1.2	0.56	2.0	1.8	4.8	1.9
Zr	14.2	16.9	71.3	25.3	16.8	29.1	18.0	14.2	49.8	26.0	12.6	13.1	21.8
Hf	0.67	0.59	2.5	1.5	1.1	1.8	1.1	1.1	3.5	1.5	1.2	1.3	1.3
Eu	0.44	0.35	1.5	0.12	1.3	1.0	0.28	0.45	0.19	0.70	0.60	1.4	0.62
Ti	866	1061	1041	2211	254	1906	855	1116	1647	851	744	508	1045
Gd	0.87	0.59	2.6	0.27	4.0	2.3	0.60	1.0	0.47	1.6	1.2	3.5	1.1
Tb	0.08	0.04	0.25	0.03	0.47	0.22	0.07	0.12	0.06	0.19	0.13	0.41	0.08
Dy	0.29	0.14	0.87	0.17	1.9	0.85	0.28	0.45	0.28	0.79	0.55	1.8	0.27
Y	0.75	0.35	2.5	0.45	5.3	2.5	0.85	1.4	0.87	2.4	1.5	5.6	0.8
Ho	0.03	0.02	0.11	0.02	0.24	0.11	0.03	0.06	0.04	0.11	0.07	0.26	0.04
Er	0.04	0.02	0.20	0.03	0.39	0.17	0.06	0.10	0.07	0.20	0.1	0.47	0.05
Tm	0.003	0.01	0.01	0.005	0.04	0.02	0.009	0.01	0.01	0.02	0.01	0.05	0.01
Yb	0.02	0.03	0.10	0.02	0.15	0.07	0.03	0.05	0.06	0.11	0.07	0.27	0.02
Lu	0.002	0.002	0.01	0.003	0.02	0.01	0.004	0.007	0.004	0.01	0.01	0.04	0.002
Eu*	1.2	1.2	1.3	1.2	0.9	1.0	1.2	1.2	1.1	1.2	1.2	1.0	1.2
La/Sm	0.56	0.23	0.44	0.35	0.27	2.93	0.18	0.20	0.58	0.34	0.42	1.01	0.62
Sr*	2.6	3.4	3.4	2.3	0.9	0.4	11.3	6.4	2.0	4.3	10	1.9	4.8

b.d. = below detection limit; 1σ standard errors are found in Appendix A.
Eu*, Lu/Gd, La/Sm calculated using chondrite normalized values from McDonough and Sun (1995).
Sr* calculated using primitive mantle normalized values from McDonough and Sun (1995).
Trace element concentrations in ppm.
TE Class = trace element classification; Gabb = gabbroic; Bas = Basaltic; Pyrox = Pyroxenite; Metasom = Metasomatized.

The Voyageur clinopyroxene Pb isotopic compositions fall along the 2-stage terrestrial lead evolution curve of Stacey and Kramers (1975) and intersect the model curve at ages from approximately 2.1 to 0 Ga. Clinopyroxene from eclogite #362A have the lowest measured Pb isotope ratios ($^{206}Pb/^{204}Pb$ 14.87–14. 97 ± 0.08; $^{207}Pb/^{204}Pb$ 15.1–15. 2 ± 0.1), and intersect the Stacey-Kramers curve at a model age of 2.1 Ga (Fig. 7b). Interestingly, clinopyroxene from eclogite #362B contains variable Pb isotope compositions, with $^{206}Pb/^{204}Pb$ varying from

15.05 to 16.57 and $^{207}Pb/^{204}Pb$ from 15.23 to 15.56, where the lower ratios intercept the Stacey-Kramers curve at approximately 2 Ga (Fig. 7b). Clinopyroxene from xenoliths #370, 383A, 408 and 395 intersect the Stacey-Kramers curve at model ages of ca. 2.0, 1.8, 1.3 and 1.2 Ga (Fig. 7c), respectively, and have associated errors of maximum ±0.23 and ±0.1 for $^{206}Pb/^{204}Pb$ and $^{207}Pb/^{204}Pb$, respectively. Linear regression of Pb isotope data from these 6 samples produce a secondary isochron with a calculated age of 2500 ± 410 Ma (2σ, MSWD = 5.1). In comparison, clinopyroxene from eclogites #378 and #346 have much higher Pb isotope ratios ($^{206}Pb/^{204}Pb$ 17.2–20.7; $^{207}Pb/^{204}Pb$ 15.4–17.1) with large uncertainties (±0.47–1.2 and ±0.41–1.0, respectively) due to much lower Pb concentrations. These results are similar to the Pb isotopic composition of the Voyageur kimberlite in Fig. 7a (Table 5).

6. Bulk eclogite reconstructions

6.1. Major elements

Kimberlite infiltration and alteration obscures whole-xenolith compositions, and bulk compositions are generally calculated from estimations of mineral modes and measured mineral compositions (e.g. Aulbach et al., 2007; Barth et al., 2001; Schmidberger and Francis, 2001). Uncertainties in mineral modes resulting from coarse grain sizes, mineral nugget effects, and small xenoliths can produce significant errors, particularly for estimated major element whole-rock compositions (e.g. Smart et al., 2014), but normalized trace element patterns (not abundances) are relatively unaffected by up to 30% fluctuations in mineral modes (Jerde et al., 1993). In order to account for the small size of the Voyageur eclogites (approximately 2–6 cm in diameter) and the relatively coarse grain size (up to 0.5 cm), and the fact that garnet-clinopyroxene abundances in eclogite are roughly subequal (e.g. Green and Ringwood, 1967; Jacob, 2004), we have chosen a blanket 50% garnet and 50% clinopyroxene mineral assemblage for the estimated whole-rock major and trace element compositions for all eclogites. In a recent review, Aulbach and Jacob (2016) choose modes of 55% garnet and 45% clinopyroxene for bulk calculations, partially based on the assumption of Archean protolith crystallization from picrite melts. However, given the Voyageur eclogites are Paleoproterozoic, a different parental melt composition is probably required, which may affect the relative abundances of garnet vs. clinopyroxene. In the reported literature, eclogite garnet-clinopyroxene mineral abundances commonly range between 50–60% and 50–40% (Aulbach and Jacob, 2016), which justifies our choice of equal garnet-clinopyroxene modes. The pyroxenite samples #383A and #383B have much higher abundances of clinopyroxene, (Fig. 2d,e), and thus modes of 20% garnet and 80% clinopyroxene were applied. Pyroxenite #393 contains orthopyroxene, so a modal assemblage of 20% garnet, 75% clinopyroxene and 5% orthopyroxene was used. Whole-rock xenolith major and trace element compositions are given in Table 6.

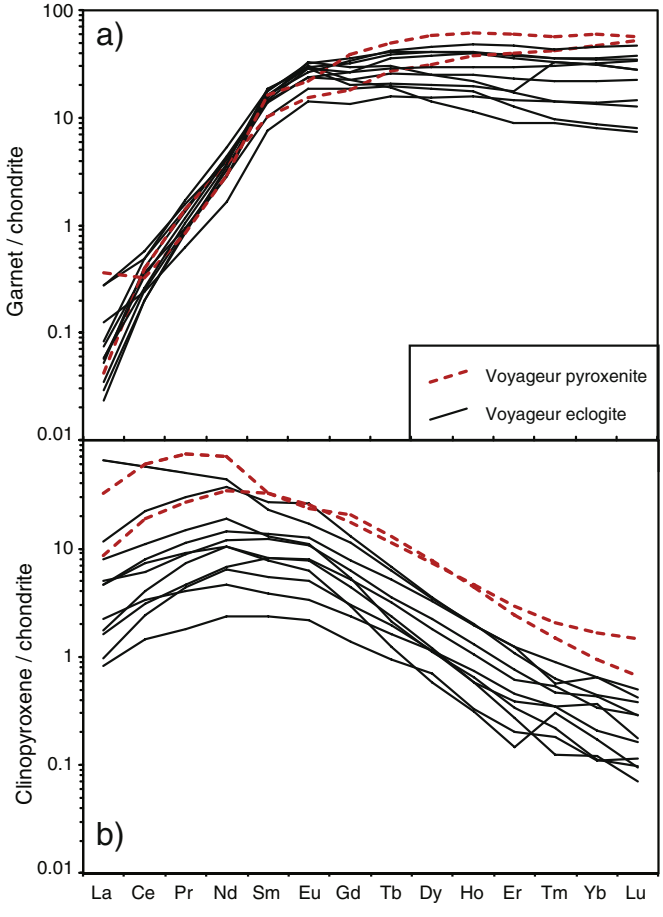

Fig. 4. Chondrite-normalized REE patterns for (a) garnet and (b) clinopyroxene from Voyageur xenoliths. Normalizing values from McDonough and Sun (1995).

The calculated whole-rock compositions of the Voyageur xenoliths are shown in Fig. 8. The eclogites contain 46.2–48.5 wt.% SiO_2, 13–20 wt.% Al_2O_3, 8.5–19 wt.% FeO, 4.8–12 wt.% MgO, 9.5–14 wt.% CaO and 2.2–4.5 wt.% Na_2O (K_2O contents are <0.01 wt.%), and are basaltic in composition. The pyroxenites have distinctly lower Al_2O_3 (5–7 wt.%) and higher CaO (17 wt.%) and SiO_2 (51 wt.%) contents compared to the eclogites, but have MgO (11–12 wt.%) and Na_2O (2–3 wt.%) contents that partially overlap with the eclogites. The Voyageur eclogites are compositionally similar to eclogite xenoliths from the nearby Jericho kimberlite (Kopylova et al., 1999a; Smart et al., 2014), but do not have as high MgO contents (e.g. Heaman et al., 2006; Smart et al., 2009). The eclogites display a negatively sloping trend between MgO and Al_2O_3 and MgO and Na_2O (Fig. 8a,c), and a positive trend is observed between MgO and Ni (not shown). The eclogites also display some compositional overlap with modern gabbros in terms of MgO, Al_2O_3, CaO, Na_2O and Ni, but the eclogites have much higher FeO and lower SiO_2 content than oceanic gabbros (Fig. 8b, d), and instead overlap with ophiolitic gabbros. Compared with modern MORB, the Voyageur eclogites have broadly overlapping CaO contents, but extend to both higher and lower Al_2O_3, FeO and MgO contents (Fig. 8). For a given MgO content, the eclogites have systematically higher Na_2O and lower SiO_2 contents (Fig. 8c, d). The Voyageur pyroxenites do not show the similarity to oceanic rocks observed in the Voyageur eclogites (Fig. 8), and instead have similar MgO, FeO and Na_2O contents as garnet pyroxenites found in ultramafic massifs.

6.2. Trace elements and eclogite classes

Calculated whole-rock REE compositions of the Voyageur xenoliths are plotted in Fig. 9. Note that the sensitivity of calculated bulk compositions has been investigated by varying the modal abundance of garnet and clinopyroxene by 10% for one sample of each xenolith class (shaded areas in Fig. 9). While the relative abundance of REEs changes, the overall patterns remain relatively constant. The pyroxenites (#383A, 383B and 393) have distinct trace element signatures compared to the eclogites, displaying weakly sinusoidal REE patterns with variably enriched $LREE_N$ and $HREE_N$ (ΣHREE = 4.5–5.7). Pyroxenite #383A displays some HREE fractionation from Er to Lu and no Eu anomaly ($Eu^* = 1.0$), while #393 has relatively flat $HREE_N$ and a small negative Eu anomaly ($Eu^* = 0.9$). Trace elements were not measured in orthopyroxene, but its exclusion will not significantly affect bulk compositions due to typically low trace element abundances (Pearson et al., 2014). The pyroxenites additionally have comparatively high Ni (160–184 ppm) contents. The chondrite-normalized REE patterns of the Voyageur eclogites, in contrast, display flat or depleted HREE patterns (Lu_N/Gd_N = 0.3–1.1), small positive Eu anomalies (Eu^* = 1.1–

Table 3
Thermobarometry and oxybarometry of Voyageur xenoliths.

Location	Sample	Trace element classification	T_{E79} (°C)	P_{B15} (kbar)	$T_{EG79\ (Geotherm)}$ (°C)	P_{V06} kbar	log fO_2 (ΔFMQ)
Voyageur	346	Gabbroic	980	42	1011	51	−3.0
Voyageur	362A	Gabbroic	923	40	943	46	−2.0
Voyageur	362B	Gabbroic	961	–	951	47	−4.6
Voyageur	380A	Gabbroic	1156	59	1171	63	−2.5
Voyageur	390	Gabbroic	873	34	902	43	
Voyageur	361	Metasomatised basaltic	1198	57	1233	68	−1.9
Voyageur	370	Basaltic	957	–	946	46	−2.1
Voyageur	378	Basaltic	945	–	931	45	−2.5
Voyageur	380B	Basaltic	1197	59	1226	68	
Voyageur	386A	Basaltic	911	46	904	43	
Voyageur	408	Basaltic	949	–	936	46	−2.5
Voyageur	383A	Pyroxenite	934	–	914	44	−3.2
Voyageur	383B	Pyroxenite	873	34	907	44	
Voyageur	393	Pyroxenite	880	–	846	39	
Voyageur	395	n/a	961	–	951	47	−2.3
Voyageur	352	n/a	998	44	1025	52	
Voyageur	376	n/a	1058	55	1057	55	−1.5
Voyageur	342	n/a	970	48	971	48	
Voyageur	344	n/a	962	39	997	50	
Voyageur	392	n/a	998	49	1002	51	
Voyageur	409	n/a	998	48	1008	51	
Voyageur	374	n/a	984	58	947	47	
Jericho	JDF6N#2	–			982	45	−2.1
Jericho	JD40MX103	–			1015	47	−4.2
Jericho	LGS10MX17	–			960	45	−2.3
Jericho	LGS25MX11	–			1095	49	2.3
Jericho	JD67MX2	–			940	44	−1.2
Jericho	JD35MX27	–			988	46	−1.5
Jericho	LGS44MX9	–			1165	52	−1.3
Muskox	10223	–			957	45	−1.6
Muskox	10334	–			949	44	−2.1
Muskox	TRS10288	–			1190	52	−0.5
Muskox	10289clean	–			968	45	−2.3
Muskox	TRS10337	–			931	44	−1.5
Muskox	TRS10283	–			955	45	−1.4

P_{B15} calculated using Beyer et al. (2015); T_{EG79} calculated using Ellis and Green (1979).
$T_{geotherm}$ and P_{V06} calculated iteratively from the peridotite geotherm in Verigeanu (2006).
P, T and $Fe^{3+}/\Sigma Fe$ data for the Jericho and Muskox eclogites from Kopylova et al. (2016).
Jericho and Muskox P-T calculated as T_{EG79} and intercept with Jericho peridotite geotherm.
Oxygen fugacity for all northern Slave samples calculated after Stagno et al. (2015) with $TG_{eotherm}$ & $P_{V06/Geotherm}$.

1.5) and overall LREE-depleted patterns (La_N/Sm_N = 0.05–0.4; excluding altered eclogite #361).

The Voyageur eclogites form two groups based on the shape of REE_N patterns, and show some similarities with the Jericho eclogites. Five eclogites (#346, 362A, 362B, 380A and 390) are characterized by positively sloped LREEs and negatively-sloped HREEs (Lu_N/Gd_N = 0.3–0.6; Lu_N = 4–14), with a distinctive peak at Eu (Eu* = 1.3–1.5). The REE_N pattern of this group is similar to that observed in oceanic gabbros, and thus these eclogites will be termed "gabbroic". The second group (#370, 378, 380B, 386A and 408) is characterized by flat but higher concentrations of HREEs (Lu_N/Gd_N = 0.9–1.1; Lu_N = 11–42), with weaker Eu* (1.1–1.3) and this group will be termed "basaltic". The "gabbroic" and "basaltic" classes correspond exactly to the textural "massive" and "foliated" groupings described in Section 4. The metasomatised eclogite #361 also belongs to the basaltic group due to the flat HREE pattern, regardless of the LREE enrichment. The gabbroic eclogites have in general lower Y (maximum 15 ppm), Sc (18–41 ppm) and ΣHREE (1.9–3.6 ppm) compared to the basaltic eclogites (Y = 17–33 ppm; Sc = 41–67 ppm; ΣHREE = 5–10). The Voyageur gabbroic eclogites correspond to the "peaked" and the basaltic to the "depleted" Jericho eclogite groups of Smart et al. (2014). This REE-based grouping also divides the eclogites based on major element composition; based on garnet composition (Fig. 3a) gabbroic eclogites classify as group "B" and the basaltic eclogites as group "C". Furthermore, the gabbroic eclogites have higher MgO contents and tend to have lower FeO contents than the basaltic eclogites (Fig. 8b). Aulbach and Viljoen (2015) and Aulbach et al. (2016) first used "basaltic" and "gabbroic" terminology for classifying eclogites from the Lace kimberlite (South Africa), and specifically grouped eclogites based on the presence of Eu anomalies and ∑REE contents, and our grouping used here is similar.

7. Discussion

7.1. The effect of metasomatism

Cratonic mantle xenoliths are susceptible to metasomatism due to protracted residence within the CLM (e.g. Jacob and Foley, 1999; Richardson et al., 2001; Schmidberger et al., 2005) and entrainment in reactive kimberlite and related magmas. Metasomatism can obscure primary geochemical and isotopic characteristics of the CLM (e.g. Heaman et al., 2006; Kelemen et al., 1998; Schmidberger and Francis, 2001; Tappe et al., 2011), and therefore possible effects of metasomatism on the composition of the Voyageur xenoliths will be evaluated.

The Voyageur pyroxenites do not show extensive alteration or kimberlite infiltration in hand specimen, and examination of clinopyroxene reveals minimal alteration (Fig. 2e, f). The Voyageur eclogites, on the other hand, show variable amounts of alteration (Fig. 2a–b). Some eclogite xenoliths are remarkably fresh, bearing clear clinopyroxene and garnet (e.g. #362A, 362B), while others possess thicker alteration rims on garnet and clinopyroxene; variably cloudy clinopyroxene (e.g. #395, #378) and infiltrating veins of carbonate material (e.g. #408, 361, 390). Some samples (e.g. #380A) contain coarse apatite, which may be related to modal metasomatism (e.g. Rudnick et al., 1993; O'Reilly and Griffin, 2000).

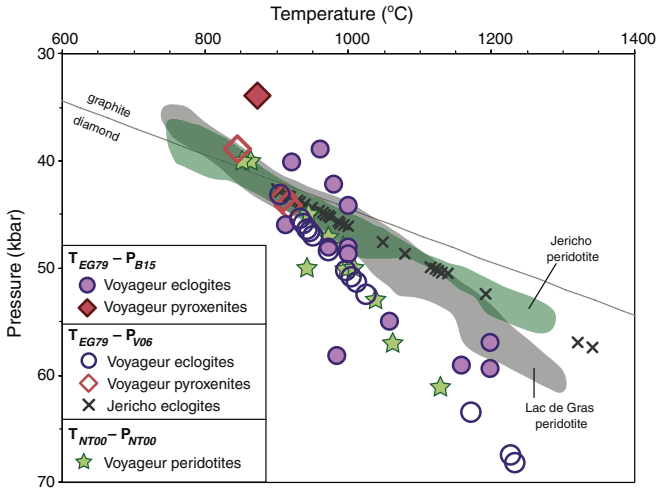

Fig. 5. Estimated pressure-temperature conditions for the Voyageur xenoliths. Closed circle and diamond symbols have temperatures calculated after Ellis and Green (1979) ("T_{EG79}") and pressures after Beyer et al. (2015) ("P_{B15}"). Open circle and diamond symbols are a combination of T_{EG79} and pressures iteratively calculated from the Voyageur peridotite array (P_{V06}). The Voyageur P-T was calculated using the single clinopyroxene thermometer and barometer from Nimis and Taylor (2000; P_{NT} and T_{NT}) and is taken from Verigeanu (2006). Shown for comparison are eclogites ($T_{EG79} - P_{V06}$; Smart et al., 2009, 2014) and peridotites (P_{NT} and T_{NT}; Grütter, 2009) from the nearby Jericho kimberlite, and peridotites from the Lac de Gras area in the central Slave domain (P_{NT} and T_{NT}; Grütter, 2009). Graphite-diamond transition is from (Kennedy and Kennedy, 1976).

Table 4
Oxygen isotope composition of Voyageur garnet.

Sample	Trace element classification	$\delta^{18}O$ (‰)	
346	Gabbroic	5.9	
362A	Gabbroic	5.9	
362B	Gabbroic	6	6.2
380A	Gabbroic	5.6	
361	Metasomatised basaltic	5.5	
370	Basaltic	5.7	
378	Basaltic	5.8	5.9
380B	Basaltic	5.7	
386A	Basaltic	5.2	
408	Basaltic	5.5	
383A	Pyroxenite	5.6	
383B	Pyroxenite	5.9	
393	Pyroxenite	5.6	
395	n/a	5.8	
376	n/a	5	
344	n/a	5.5	

$\delta^{18}O$ values are relative to VSMOW.
2σ on all analyses is 0.16 ‰.
n/a = trace elements not collected.

The rarity of coarse phlogopite, rutile, and apatite (excluding #380A and 390) indicates minor modal metasomatism of the Voyageur eclogites, however, the effects of cryptic metasomatism are more difficult to identify. The chondrite-normalized REE patterns in Figs. 4 and 9 for the majority of Voyageur garnet, clinopyroxene and bulk rocks do not display pronounced incompatible element enrichments that could be attributed to metasomatism. However, garnet from eclogite #361 (clearly altered and infiltrated), eclogite #362A (very fresh), and pyroxenite #393 display elevated La and Ce contents compared to other eclogites (Fig. 4a). This LREE enrichment is mirrored in clinopyroxene from #361 (resulting in enriched calculated bulk rock REE profiles; Fig. 9a), but not in clinopyroxene from #362A and #393 (Fig. 4b). Additionally, LREE enrichments are observed in clinopyroxene from eclogite #362B and pyroxenite #383A. In order to assess trace element equilibrium between garnet and clinopyroxene, Voyageur $D^{cpx/grt}$ values are compared to $D^{cpx/grt}$ values from both experimental eclogitic (Green et al., 2000) and natural pyroxenitic (Zack et al., 1997) assemblages (Supplementary Fig. S1; c.f. Aulbach et al., 2011). Comparison of the $D^{cpx/grt}$ values indicates disequilibrium in some Voyageur xenoliths, where for some of the LREE, $D^{cpx/grt}$ is slightly elevated in #361, 362B and 383A and slightly lowered in 362A and 393.

The trace element contents of the Voyageur xenoliths are compared in Fig. 10a to eclogites with evidence of both modal and cryptic metasomatism (Jericho phlogopite ± diamond eclogites; Smart et al., 2009; Kimberley phlogopite eclogites; Jacob et al., 2009) and those without apparent overprint (Jericho bimineralic eclogites; Smart et al., 2014). The majority of the Voyageur eclogites generally has low garnet Zr

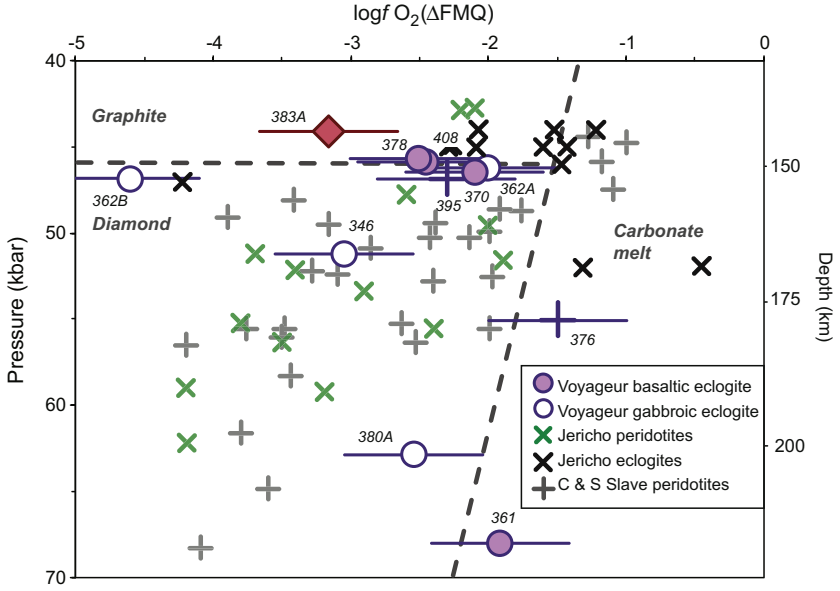

Fig. 6. Oxybarometry of Voyageur eclogite xenoliths. Pressures determined from the Voyageur peridotite paleogeotherm of Verigeanu (2006) and log$f$$O_2$ values (relative to the FMQ buffer) calculated from Stagno et al. (2015). Fields for carbonate melt, diamond and graphite redrawn from Stagno et al. (2015). Shown for comparison are eclogites from the northern Slave Jericho and Muskox kimberlites (Kopylova et al., 2016); peridotites from the Jericho and southern Slave Gahcho Kue kimberlites (McCammon and Kopylova, 2004); peridotites from the central Slave Diavik kimberlite (Creighton et al., 2009).

Table 5
Pb isotope composition of clinopyroxene from the Voyageur xenoliths.

	Trace element classification	$^{206}Pb/^{204}Pb$	2σ	$^{207}Pb/^{204}Pb$	2σ	$^{208}Pb/^{204}Pb$	2σ	$^{207}Pb/^{206}Pb$	2σ	$^{208}Pb/^{206}Pb$	2σ
346	Gabbroic	19.48	2.1	16.38	1.21	40.10	3.43	0.83	0.02	2.04	0.04
362A	Gabbroic	14.92	0.08	15.14	0.10	34.94	0.30	1.02	0.00	2.34	0.01
362B	Gabbroic	15.14	0.12	15.29	0.08	35.19	0.20	1.01	0.01	2.32	0.02
370	Basaltic	15.26	0.23	15.29	0.10	35.42	0.37	1.00	0.01	2.32	0.01
378	Basaltic	17.99	0.91	16.00	0.79	38.32	1.88	0.89	0.01	2.13	0.01
408	Basaltic	16.22	0.07	15.31	0.05	36.22	0.17	0.94	0.00	2.23	0.00
395	n/a	16.66	0.23	15.41	0.08	36.09	0.35	0.93	0.01	2.17	0.01
383A	Pyroxenite	15.59	0.20	15.31	0.06	36.11	0.39	0.98	0.01	2.31	0.01
Host kimberlite	(174 Ma)	18.78	0.019	15.61	0.016	38.66	0.039	U = 2.02 Th = 11.34 Pb = 7.67			

Reported values are averages of analyses from 6 grains; full dataset can be found in Appendix B.
U, Th and Pb contents of host kimberlite given in ppm.

and clinopyroxene Ce contents, overlapping with the bimineralic Jericho samples, and do not show strong evidence for cryptic metasomatism. However, several samples have geochemical and isotopic compositions that indicate metasomatic overprinting. Specifically, eclogites #380B and #361 have elevated Zr and Ce (Fig. 10a), and also higher TiO_2 contents in garnet (0.24–0.28 wt.% vs. <0.18 wt.%). Additionally, the variable Pb isotope compositions of the Voyageur clinopyroxene could indicate cryptic metasomatism, and for some samples (e.g. #346) high $^{206}Pb/^{204}Pb$ ratios are accompanied with elevated La_N/Yb_N (Fig. 10b; e.g. McCoy-West et al., 2016). Clinopyroxene from eclogite #362B shows variable Pb isotopic compositions (attributed to mixing with a metasomatic agent; see Section 7.2.1; Fig. 7b and Supplementary Fig. S2) and also elevated Ce and La_N/Yb_N. Together with eclogite #361 (clinopyroxene Ce = 35.1 ppm), both these eclogites have calculated whole rock $Ce_N/Yb_N > 1.6$, compared to Ce_N/Yb_N of 0.09–0.9 for all other Voyageur eclogites (Figs. 9a, b and 10b). Therefore, while some Voyageur eclogites (e.g. #361, 362B, 380B) display geochemical and isotopic enrichment indicative of selective metasomatism, the majority eclogites appear to have compositions that are largely representative of the protolith.

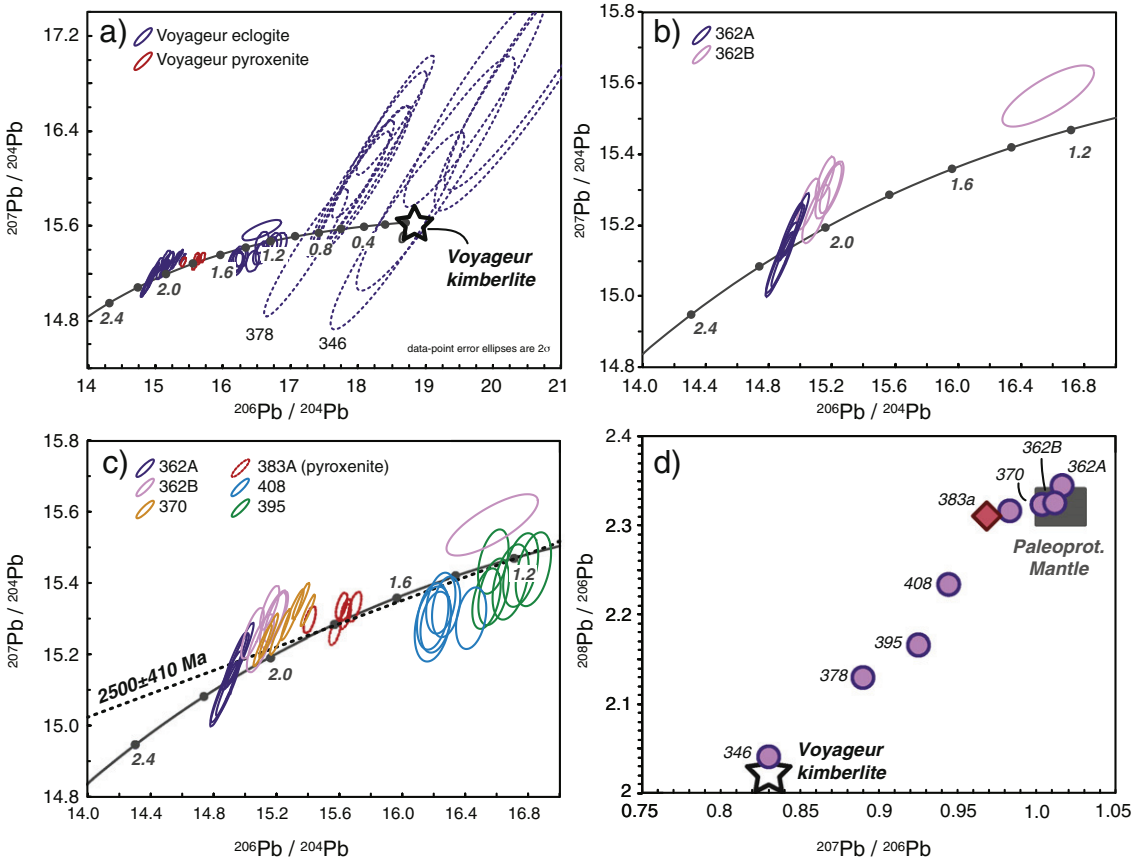

Fig. 7. Pb isotope compositions of clinopyroxene from Voyageur xenoliths. All ellipses represent one analysis and encompass the 2σ error. Two-stage terrestrial Pb growth curve from Stacey and Kramers (1975). The 174 Ma Voyageur kimberlite Pb isotopic composition is from Tappe (unpublished data). (a) $^{206}Pb/^{204}Pb$ vs. $^{207}Pb/^{204}Pb$ of clinopyroxene from studied Voyageur xenoliths. (b) $^{206}Pb/^{204}Pb$ vs. $^{207}Pb/^{204}Pb$ results from eclogite #362A and #362B, showing intersection with the Stacey-Kramers curve at ~2.1 to 2.0 Ga. While the Pb isotope ratios from #362A are relatively uniform, clinopyroxene from #362B contain a more radiogenic Pb isotope signature that is ascribed to mixing with the host kimberlite. (c) Regression of Pb isotope ratios for Voyageur eclogites and pyroxenites, excluding samples #346 and #378 (due to large uncertainties). The secondary isochron has an associated age of 2500 ± 410 Ma (2σ, MSWD = 5.1). (d) $^{208}Pb/^{206}Pb$ vs. $^{207}Pb/^{206}Pb$ showing the average isotopic values calculated for each xenolith. Mixing of Paleoproterozoic source mantle with more radiogenic kimberlite Pb appears to explain the variation in Voyageur clinopyroxene Pb isotope compositions. The Pb ratios for the kimberlite box are taken from the Voyageur kimberlite at 174 Ma (see Table 5). The Pb ratios for the Paleoproterozoic mantle are assumed to be equivalent to the oceanic crust protolith and are taken from the Stacey-Kramers 2-stage Pb model curve between 2 and 2.25 Ga.

Table 6
Calculated whole-rock composition of the Voyageur xenoliths.

	346	362A	362B	380A	390	361	370	378	380B	386A	408	383A	393
Trace element classification:	Gabbroic	Gabbroic	Gabbroic	Gabbroic	Gabbroic	Basaltic/metasomatised	Basaltic	Basaltic	Basaltic	Basaltic	Basaltic	Pyroxenite	Pyroxenite
SiO_2	47.7	48.5	48.0	47.8	47.6	47.5	48.0	47.6	47.3	46.2	47.3	51.8	51.3
TiO_2	0.16	0.14	0.12	0.28	0.10	0.36	0.14	0.18	0.27	0.18	0.12	0.1	0.1
Al_2O_3	15.7	18.0	14.5	17.9	16.3	17.1	15.7	16.2	15.7	13.0	14.3	6.9	5.2
Cr_2O_3	0.01	0.05	0.08	0.02	0.03	0.02	0.05	0.02	0.02	0.02	0.04	0.1	0.1
FeO	11.7	8.5	13.5	12.0	11.5	11.3	12.7	15.44	10.2	18.8	14.6	10.8	11.7
MnO	0.15	0.16	0.24	0.20	0.18	0.29	0.20	0.23	0.38	0.29	0.25	0.09	0.09
MgO	10.5	10.0	12.0	6.7	10.17	7.4	9.1	6.8	8.58	7.62	8.88	10.9	12.3
CaO	11.0	11.3	9.50	11.2	10.5	11.9	11.9	10.8	14.2	11.7	12.4	16.5	17.1
Na_2O	2.95	3.38	2.37	4.33	3.12	4.03	2.79	3.42	3.06	2.23	2.28	2.8	2.1
K_2O	0.01	0.01	0.01	0.00	0.01	0.01	0.01	0.01	0.01	0.01	0.01	0.0	0.0
Total	99.8	100.1	100.3	100.5	99.4	100.0	100.6	100.7	99.7	100.0	100.2	79.8	79.9
Mg#	0.66	0.73	0.64	0.55	0.66	0.58	0.60	0.49	0.62	0.45	0.55	20.8	20.7
V	104	165	298	136	464	174	261	370	277	489	426	420	282
Ni	152	75	58	22	102	42	56	31	8	31	81	160	184
Sc	19	41	40	18	95	37	42	41	67	56	58	70	22
Rb	0.01	0.51	0.30	0.14	0.04	0.15	0.02	0.01	0.02	0.01	0.06	0.05	0.18
Ba	0.25	5.8	0.55	0.09	2.2	1.4	0.24	0.08	b.d.	0.15	0.24	1.1	0.65
Th	0.01	0.04	0.02	0.00	0.05	0.34	0.01	0.01	0.01	0.01	0.01	0.08	0.02
U	0.01	0.03	0.04	0.01	0.01	0.08	bd	0.005	0.01	0.01	0.01	0.03	0.003
Nb	0.06	0.06	0.01	0.05	0.11	0.2	0.004	0.002	0.36	0.001	0.004	0.01	0.02
Ta	0.004	0.00	0.002	0.004	0.01	0.02	0.003	0.002	0.10	0.002	0.002	0.002	0.002
La	0.56	0.24	1.4	0.10	1.1	7.8	0.12	0.20	0.27	0.55	0.60	6.2	1.5
Ce	2.4	1.4	6.9	0.56	5.9	18	0.81	1.0	1.2	2.5	2.0	29	5.4
Pr	0.47	0.42	1.4	0.15	1.3	2.4	0.24	0.26	0.25	0.57	0.46	5.7	1.1
Pb	0.29	1.5	1.2	0.05	0.72	0.14	1.8	0.26	11	0.55	0.88	11	3
Sr	91	273	412	18	101	64	225	134	32	199	376	796	471
Nd	3.0	3.6	8.8	1.6	8.5	11	2.3	2.3	2.0	3.9	3.6	26	7.3
Sm	1.4	1.9	2.5	1.3	3.6	2.9	1.4	1.9	1.3	2.2	2.3	4.1	2.0
Zr	11	14	40	21	18	34	14	13	59	17	9.4	12	19
Hf	0.37	0.36	1.3	0.89	0.85	1.2	0.62	0.66	2.3	0.83	0.66	1.1	1.0
Eu	0.75	1.0	1.1	1.0	1.3	1.3	0.81	1.1	0.76	1.1	1.1	1.3	0.82
Ti	711	872	734	1554	445	1696	811	1002	1404	815	701	520	907
Gd	2.3	2.5	2.6	3.1	5.9	4.3	2.5	4.1	2.9	4.1	3.2	3.5	1.7
Tb	0.40	0.36	0.41	0.57	1.1	0.81	0.50	0.80	0.67	0.85	0.58	0.52	0.21
Dy	2.4	1.8	2.3	3.2	8.1	5.5	3.2	5.3	4.8	5.9	3.9	3.0	1.2
Y	12	7.8	12	15	45	28	17	28	25	33	21	14.4	5.7
Ho	0.50	0.32	0.48	0.61	1.8	1.2	0.71	1.1	1.1	1.4	0.85	0.62	0.24
Er	1.0	0.73	1.3	1.4	5.1	3.1	1.9	3.1	2.9	3.8	2.4	1.6	0.61
Tm	0.12	0.11	0.18	0.18	0.73	0.45	0.27	0.45	0.41	0.55	0.38	0.25	0.08
Yb	0.72	0.66	1.17	1.1	4.9	2.8	1.8	2.9	2.5	3.7	2.6	1.7	0.52
Lu	0.10	0.09	0.18	0.16	0.71	0.43	0.28	0.46	0.35	0.59	0.42	0.29	0.07
Eu*	1.3	1.4	1.3	1.4	1.5	1.1	1.3	1.2	1.1	1.1	1.2	1.0	0.9
Sr*	2.1	3.3	3.3	1.0	4.1	0.4	8.1	4.7	1.2	3.7	8.1	1.8	0.9

	383B	395	352	376	342	344	392	409	374
TE Class.	n/a	n/a	n/a	n/a	n/a	n/a	n/a	n/a	n/a
SiO_2	50.9	46.7	47.2	48.1	47.5	47.8	47.8	47.3	47.3
TiO_2	0.1	0.13	0.28	0.17	0.14	0.11	0.14	0.28	0.12
Al_2O_3	6.7	13.8	18.4	19.9	16.0	16.8	19.0	16.5	15.8
Cr_2O_3	0.1	0.01	0.01	0.01	0.05	0.07	0.02	0.01	0.04
FeO	10.9	15.6	13.0	10.5	12.7	10.2	11.6	13.9	14.8
MnO	0.09	0.27	0.19	0.14	0.19	0.19	0.16	0.31	0.30
MgO	11.1	8.94	5.30	4.76	8.69	9.85	6.32	6.50	7.68
CaO	16.6	12.1	10.7	12.1	11.8	11.5	10.4	11.6	10.5
Na_2O	2.8	2.22	4.54	4.34	2.83	2.97	4.13	3.66	3.27
K_2O	0.0	0.01	0.01	0.01	0.01	0.01	0.01	0.01	0.00
Total	79.4	99.8	99.6	100.1	100.0	99.5	99.7	100.2	99.8
Mg#	20.5	0.54	0.49	0.53	0.59	0.68	0.57	0.50	0.53

Eu* and Sr* as calculated in Table 2; trace element classification discussed in Section 6.2 and Fig. 9.
Bulk eclogite compositions are calculated with 50% grt and 50% cpx.
Bulk pyroxenite compositions are calculated with 25% grt - 75% cpx (383A) and 20% grt - 75% cpx - 5% opx (393).
Major elements contents in wt.%; trace element contents in ppm.

7.2. Origin of the Voyageur eclogites and pyroxenites

7.2.1. Age constraints

The Pb isotope compositions of Voyageur clinopyroxene extend from relatively unradiogenic compositions that intercept the Stacey-Kramers two-stage terrestrial Pb evolution curve at approximately 2.1 Ga, to more radiogenic compositions that are similar to the Jurassic Voyageur kimberlite (Fig. 7a). The discrete Pb isotope compositions determined for each Voyageur eclogite xenolith result in Stacey-Kramers model intercept ages of 2.1, 2.0, 1.8, 1.3 and 1.2 Ga (Fig. 7c). This multitude of model ages could be interpreted as punctuated eclogite and pyroxenite formation in the northern Slave CLM beneath Voyageur during

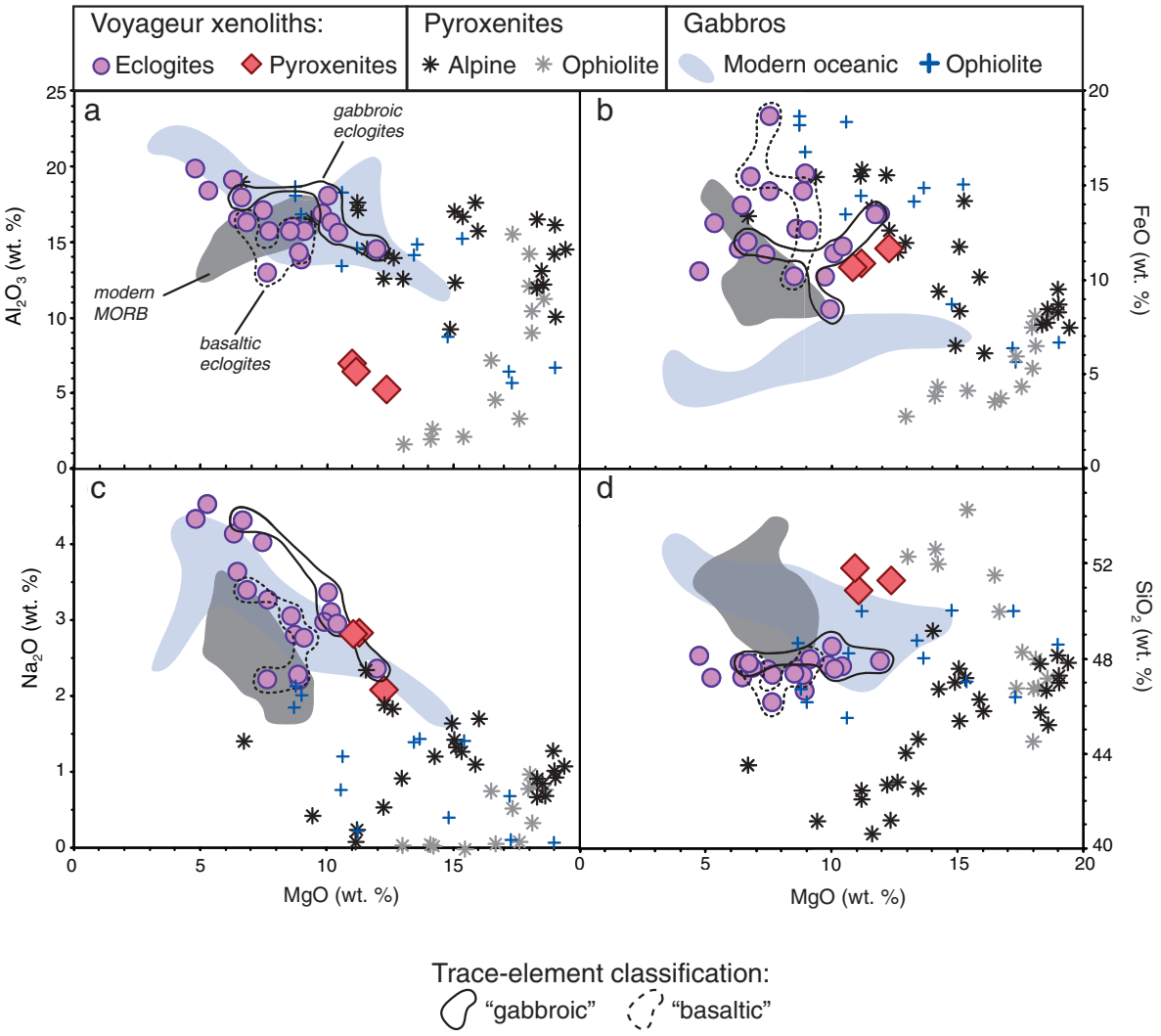

Fig. 8. Calculated whole rock compositions of the Voyageur xenoliths using the parameters defined in Table 6. The Voyageur eclogites have been put into "basaltic" and "gabbroic" groups according to calculated whole-rock trace element patterns in Fig. 9; see text for more detail. Shown for comparison are modern MORBs (Jenner and O'Neill, 2012); altered modern ocean gabbros (Bach et al., 2001); gabbros and pyroxenites from ophiolites (Bodinier and Godard, 2003; Monnier et al., 2003) and pyroxenites from alpine massifs (Garrido et al., 2006; Gysi et al., 2011).

the Paleo- to Mesoproterozoic. However, our preferred interpretation, which is in line with previous interpretations of isochron and model ages obtained for the Jericho (1.7–2.2 Ga; Schmidberger et al., 2005; Smart et al., 2014) and Lac de Gras area eclogites (1.8–2.4 Ga; Aulbach et al., 2009a, 2009b; Schmidberger et al., 2007), is that the least radiogenic isotope compositions of the Voyageur clinopyroxenes represent formation of the Voyageur eclogite and pyroxenite protoliths during the Paleoproterozoic. At temperatures appropriate for the lower CLM (e.g. 900 °C), Pb isotope compositions can be retained in 1 mm clinopyroxene grains for 10 Myr timescales, owing to the relatively slow diffusion of Pb in clinopyroxene (Cherniak, 2001). The selected Voyageur xenoliths have T_{EG79} ranging from 914 to 1011 °C and clinopyroxene grain sizes from 0.5 to 2 mm; therefore, contact with high-μ rocks or metasomatic agents should not overprint clinopyroxene unless grains are exposed for prolonged timescales or at elevated temperatures. Additionally, while the Voyageur clinopyroxene have low measured U/Pb ratios (0.002–0.03), the protoliths (interpreted as oceanic rocks in the following section) may have had higher U/Pb ratios and μ-values (average MORB U/Pb ~0.20 and μ-values ~11; Jenner and O'Neill, 2012; White, 1993), resulting in isotopic ingrowth for 100–200 Myr before subduction of the oceanic crust (e.g. Smart et al., 2014). Fluid loss and partial melting during subduction and transformation of oceanic crust to eclogite and pyroxenite would have lowered the U/Pb of the Voyageur oceanic protoliths (e.g. Klemme et al., 2002; Tappe et al., 2011), and should have resulted in effectively unchanged clinopyroxene Pb isotope compositions since time of subduction, i.e. since the Paleoproterozoic in our model.

However, it should be noted that CO_2-rich, mantle metasomatic agents with "high-μ" (high $^{238}U/^{204}Pb$ ratio) signatures may overprint the Pb isotopic composition of the lithospheric mantle over relatively short (< 200 Myr) timescales (e.g. McCoy-West et al., 2016). Thus, the preservation of unradiogenic Pb signatures in some Voyageur clinopyroxene indicates either interaction with a metasomatic agent was brief (e.g. shortly preceeding or concomitant with Jurassic kimberlite magmatic activity), or the composition of the clinopyroxene and equilibrium PT conditions prevented fast Pb diffusion (e.g. Cherniak, 2001). Additionally, the clinopyroxenes that display more radiogenic Pb isotope signatures (e.g. #346 and #378) have very low Pb contents (0.4 and 0.5 ppm, vs. 1.9 to 13.3 ppm), which possibly made these samples more susceptible to overprinting.

Hence, assuming that the least radiogenic Pb isotope ratios for the clinopyroxene record that of the protolith, Voyageur eclogite and pyroxenite formation occurred during the Paleoproterozoic. If the clinopyroxene Pb isotope data represents a secondary isochron (Fig.

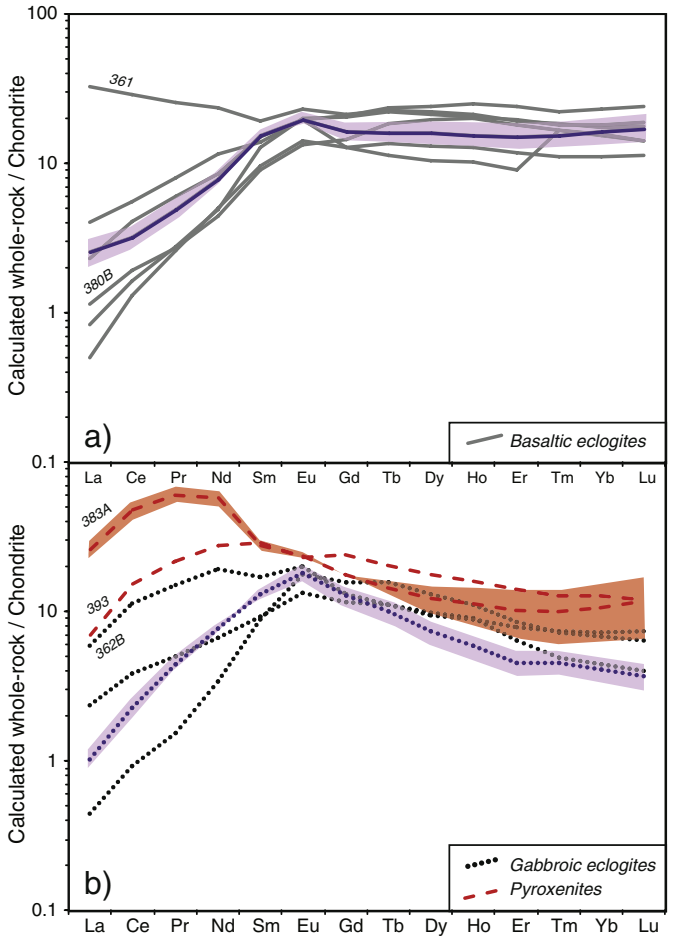

Fig. 9. Calculated whole rock rare earth element profiles of the Voyageur xenoliths using the modal abundances detailed in Fig. 8 and in the text. The Voyageur eclogites are grouped according to whole-rock REE pattern; see text for details. "Gabbroic" eclogites have dotted lines, "basaltic" eclogites have solid lines, and pyroxenites have dashed lines. The effect of changing the modal abundances by 10% on the calculated bulk composition is shown by the shaded field each of the three rock types. Eclogite #361 displays an enriched "metasomatised" pattern but would otherwise fall into the "basaltic" category. Chondrite normalization values from McDonough and Sun (1995).

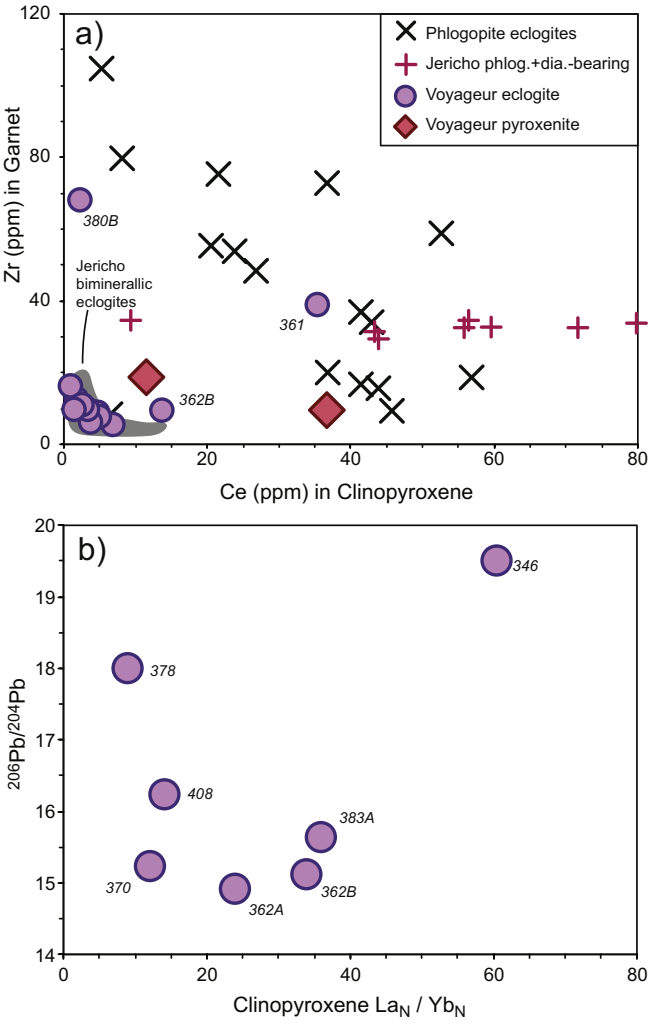

Fig. 10. Constraining the degree of cryptic metasomatism in the Voyageur eclogites. (a) Garnet Zr and clinopyroxene Ce contents in ppm. Kimberley (Kaapvaal craton) phlogopite-bearing eclogites from Jacob et al. (2009); Jericho phlogopite ± diamond and bimineralic ("barren") eclogites from Smart et al. (200; 2014). (b) Comparing the degree of LREE-enrichment, represented here by chondrite-normalized La/Yb, present in clinopyroxene with Pb isotopic signature. Normalizing values from McDonough and Sun (1995).

7c), then regression of all data (excluding eclogites #378 and #346 with kimberlitic Pb) yields an age of 2500 ± 410 Ma (MSWD = 5.1), which is within error of the oldest model age of 2.1 Ga. However, the spread in Pb isotope compositions more likely resulted from mixing with a relatively young mantle metasomatic agent, such as a low-degree, volatile-bearing ultramafic melt, potentially related to Jurassic kimberlite magmatism (cf., Hunt et al., 2012; Schmidberger et al., 2007; Smart et al., 2014; Tappe et al., 2011). Kimberlite-eclogite Pb mixing is supported by the variable Pb isotope composition of #362B (Fig. 7b), the correlations between $^{208}Pb/^{206}Pb$–$^{207}Pb/^{206}Pb$ (Fig. 7d) and Pb content and $^{206}Pb/^{204}Pb$ ratios ($r^2 = 0.67$; Supplementary Fig. S2). The Pb isotope compositions of clinopyroxene from #362A and #362B are the most unradiogenic and intercept the Stacey-Kramers curve between 2.1 and 2.0 Ga (Fig. 7b). While #362A clinopyroxene has very uniform isotopic compositions ($^{206}Pb/^{204}Pb = 14.9 \pm 0.1$ and $^{207}Pb/^{204}Pb = 15.2 \pm 0.1$), #362B clinopyroxene shows evidence of mixing with the host kimberlite, with preservation of both low $^{206}Pb/^{204}Pb$ values around 15.05 and higher $^{206}Pb/^{204}Pb$ values of 16.57 (Fig. 7b). A mixing model between the inferred "protolith" Paleoproterozoic oceanic crust and the host Jurassic kimberlite (Supplementary Fig. S2) demonstrates that most of the Voyageur clinopyroxenes contain <5% kimberlite contamination, and only samples #346 and #378 (i.e., those with the lowest Pb contents and largest associated uncertainties; Fig. 7a) show more significant (>20%) kimberlite addition. In summary, we interpret that the least radiogenic clinopyroxene Pb isotope compositions and their intercept with the Stacey-Kramers model curve at ca. 2.1 Ga, defines the minimum age of the Voyageur mafic xenoliths suite.

7.2.2. Formation as fragments of Proterozoic oceanic lithosphere

The Voyageur gabbroic and basaltic eclogites, based on their geochemical features, are interpreted to have protoliths within the oceanic lithosphere, which is in agreement with the majority of eclogite xenolith studies (e.g. Jacob, 2004; Aulbach and Jacob, 2016; but see Griffin and O'Reilly, 2007 for an opposing viewpoint). If the Voyageur eclogites do represent Paleoproterozoic oceanic crust, then they have the same origin as eclogitic material from the Jericho and Lac de Gras kimberlites (e.g. Aulbach et al., 2009a, 2009b, 2011; Heaman et al., 2002; Schmidberger et al., 2005, 2007; Smart et al., 2014), and are linked to the formation and subduction of oceanic lithosphere that accompanied ca. 1.9 Ga arc accretion and collision during the Paleoproterozoic Wopmay orogeny (Hildebrand et al., 1987).

The reconstructed bulk eclogite REE compositions of both gabbroic and basaltic Voyageur eclogites show variable amounts of LREE depletion and presence of positive Eu anomalies (Fig. 9). However, the two

groups of Voyageur eclogites are distinguished by several geochemical features. The gabbroic eclogites have reconstructed bulk trace element patterns with prominent positive Eu and Sr anomalies (Eu* up to 1.3; Sr* up to 8.1; see Table 6) and marked depletions in the HREEs (Fig. 9b). These features are similar to modern oceanic gabbros (Fig. 11a). In contrast, the basaltic eclogites display flat HREE patterns (Fig. 9a) that are reminiscent of the extrusive portion of oceanic lithosphere (Fig. 11b). The whole-rock compositions of the gabbroic eclogites tend to both overlap with and follow trends observed in oceanic gabbros in terms of MgO, Al_2O_3 and Na_2O (Fig. 8a, c), although the gabbroic eclogites have much higher estimated FeO contents (Fig. 8b). In general, the basaltic eclogites have comparatively lower MgO contents, and major element compositions that partially overlap with modern MORB (Fig. 8). Further evidence for distinctly different oceanic protoliths for the Voyageur eclogites is shown in Fig. 12, where the basaltic eclogites have higher Y and HREE contents, overlapping with modern MORB, whereas the gabbroic eclogites show clear affinities to oceanic gabbroic rocks.

Both types of Voyageur eclogites have lower SiO_2 contents compared to MORB, Archean basalts and gabbros (Fig. 8d), a feature that is typical for cratonic mantle eclogite xenoliths (Jacob, 2004), and has been attributed to loss of partial melt during subduction of the mafic oceanic protolith (e.g. Barth et al., 2001; Ireland et al., 1994; Jacob and Foley, 1999; Tappe et al., 2011). Trace element modeling shows that >20% partial melt loss in the garnet stability field can partially account for LREE depletion in the basaltic eclogites (Fig. 11b), but the relative enrichment MREEs is inconsistent with this partial melting model. The MREE contents of the basaltic eclogites could have been influenced by flushing of the basaltic portion of a subducting slab with serpentinite-derived fluids (likely from within the same downgoing slab), as was proposed for central Slave craton eclogites containing significantly fractionated MREE patterns (Aulbach et al., 2011). However, the Voyageur basaltic eclogites do not show the same extreme MREE patterns as their central Slave analogs (Fig. 11b). If partial melt extraction caused the observed HREE depletion in the gabbroic eclogites, post-eclogitization melting is excluded, because this would result in flat- or slightly-enriched HREEs within the eclogitic residue (e.g. Fig. 11b). Melting of oceanic gabbros at crustal pressures (~1 GPa) can be excluded based on the relatively cool nature of subduction-zone geotherms (e.g. Schmidt and Poli, 2014), but it has been demonstrated both experimentally and in field studies that oceanic gabbros may locally melt in shear zones in the presence of water-rich fluids (Koepke et al., 2004, 2014). Partial melting of gabbro protoliths at shallow, crustal pressures (leaving a plagioclase-pyroxene-olivine residue; Fig. 11a) does effectively result in LREE depletions in the residue, however, HREEs in the residue remain fairly unfractionated. Thus, the variable REE depletion observed in the gabbroic eclogites probably results from trace element fractionation that accompanies accumulation of plagioclase ± pyroxene ± olivine during gabbro crystallization within the oceanic crust (Jacob and Foley, 1999; Aulbach and Viljoen, 2015), which is known from both modern (e.g. Bach et al., 2001) and ophiolitic oceanic gabbros (e.g. Benoit et al., 1996; Peltonen et al., 1998).

Generally, the oxygen isotope compositions of garnet (± clinopyroxene) from eclogite xenoliths are regarded as key evidence to confirm crustal protoliths for mantle xenoliths (Jacob, 2004). Eclogitic minerals often have $\delta^{18}O$ values both above and below the mantle range of 5.1–5.9‰ (Barth et al., 2001; Dongre et al., 2015; Jacob et al., 1994; MacGregor and Manton, 1986; Pernet-Fisher et al., 2014; Riches et al., 2010; Schulze et al., 2000; Smart et al., 2014; Tappe et al., 2011), which reflects interaction with low-temperature seawater in an oceanic setting (e.g. Eiler, 2001). Eclogitic garnets from the nearby Jericho kimberlite have a relatively small range of $\delta^{18}O$ values between 5.3 and 6.6‰ (Smart et al., 2012, 2014), and garnets from the Voyageur eclogites have an even more restricted range of $\delta^{18}O$ values from 5.2 to 6.2‰ (Table 4). Eclogite #362B contains garnet with $\delta^{18}O$ values >6‰ that fall outside the accepted mantle range of 5.5 ± 0.4‰

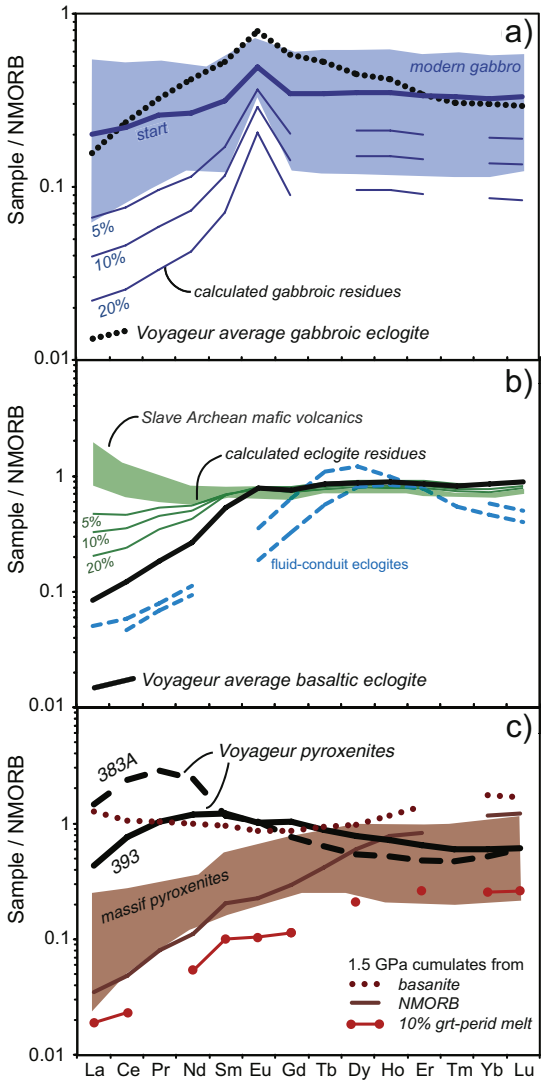

Fig. 11. NMORB-normalized REE modeling of the petrogenesis of the Voyageur eclogites and pyroxenites. Representative profiles are shown for a gabbroic eclogites in (a), basaltic eclogites in (b) and pyroxenites in (c). (a) Comparison of representative Voyageur gabbroic eclogites to average modern oceanic gabbros (blue field; Bach et al., 2001). Low-pressure (plagioclase + clinopyroxene + olivine) residues of between 5 and 20% partial melt extraction from an average gabbro (thick blue line) are displayed. Partition coefficients from Norman et al. (2005). (b) Comparison of representative Voyageur basaltic eclogite to Slave craton Archean mafic volcanics (green field; Yamashita et al., 1999). Between 5 and 20% batch melts were extracted at 3 GPa from the average basalt of Yamashita et al. (1999) using the partition coefficients from Barth et al. (2002). Examples of "fluid-conduit" eclogites from Aulbach et al. (2011) are shown for comparison. (c) Comparison of Voyageur pyroxenites to select massif pyroxenites from Gysi et al. (2011). Plagioclase-bearing garnet pyroxenite (10% plagioclase–20% garnet–70% clinopyroxene; partition coefficients from Green et al., 2000 and Bindemann et al., 2000; c.f. Smart et al., 2012) in equilibrium with a basanite (Tappe et al., 2007), average NMORB (Gale et al., 2013) and 10% melt of garnet-bearing depleted mantle are shown for comparison (partition coefficients and depleted mantle composition from Stracke et al., 2003). NMORB values from Gale et al. (2013).

(Mattey et al., 1994), which is evidence in favor of an altered oceanic crust protolith. However, it must be noted that the remainder of garnet $\delta^{18}O$ values that are "mantle-like" do not preclude protolith formation within oceanic crust (e.g. Schmickler et al., 2004), because not all oceanic crust displays $\delta^{18}O$ values fractionated from fresh MORB (5.5‰; e.g. Eiler, 2001). Oceanic rocks with "mantle-like" oxygen isotope compositions occur in the sheeted dykes where the transition from low- to high-temperature seawater interaction takes place (Alt et al., 1986; Alt and

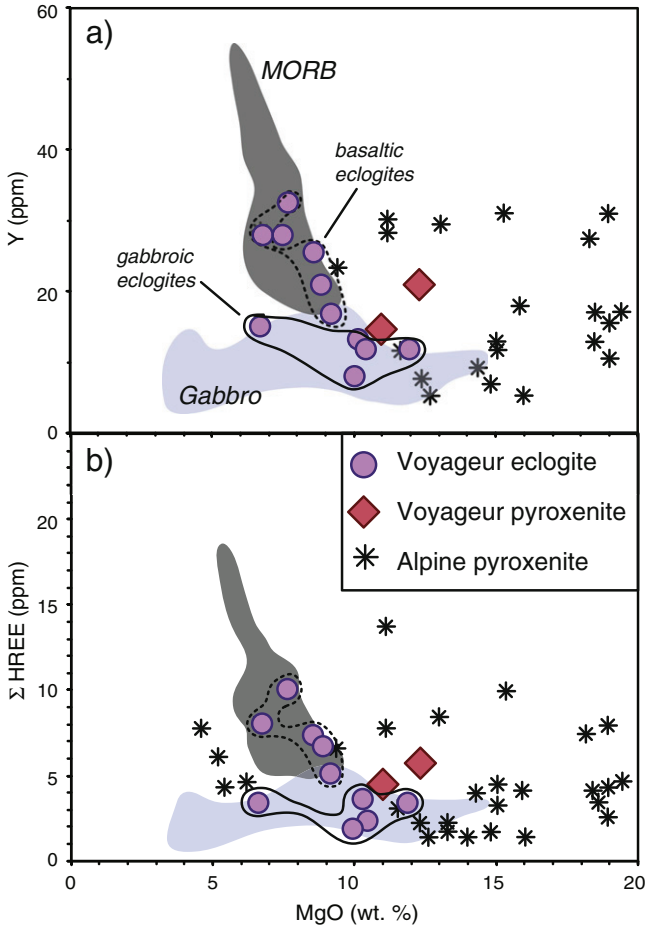

Fig. 12. (a) MgO vs. Y (b) MgO vs. ΣHREE of Voyageur gabbroic eclogite, basaltic eclogite and pyroxenite calculated whole-rock compositions with comparison to oceanic rocks and crustal pyroxenites. References for comparison fields are in Fig. 8.

Teagle, 2000), or in the lower oceanic gabbros that either undergo high-temperature alteration (with limited isotope fractionation) or are beyond the reach of seawater penetration (e.g. Hart et al., 1999; Alt and Teagle, 2000). Eclogite protoliths that formed in these portions of the oceanic crust may, therefore, not exhibit fractionated $\delta^{18}O$ values (c.f. Schmickler et al., 2004; Smart et al., 2012).

7.2.3. Origin of Voyageur pyroxenites

The Voyageur pyroxenite xenoliths have several distinct compositional characteristics from the eclogites and, thus, must have had a somewhat different petrogenesis. Firstly, the 3 pyroxenite samples record the lowest equilibration pressures and temperatures of all Voyageur mantle xenoliths, being spatially restricted to between 130 and 150 km depths (Fig. 5). Secondly, the pyroxenite calculated bulk compositions show sinusoidal patterns with enriched LREEs, slight negative Eu anomalies (e.g. #393), variable Sr anomalies, negatively sloping MREEs, and some minor HREE fractionation (e.g. #383A; Fig. 9b). Thirdly, their major element compositions do neither correspond to common global basaltic compositions nor to low-pressure gabbroic cumulates (Fig. 8). Rather, they have some compositional similarities to pyroxenitic layers and veins in both ophiolites and continental ultramafic massifs (e.g., Garrido et al., 2006; Gysi et al., 2011; Pearson et al., 1993; Figs. 8 and 12). However, alpine pyroxenite trace element patterns are typified by strongly fractionated HREEs (Yb_N/Gd_N up to 5.4) and high Y contents (up to 61 ppm), which contrasts with the trace element patterns of the Voyageur pyroxenites (Figs. 11c, 12). It has been suggested that mantle pyroxenites represent hybrid rocks produced during reactions between eclogite-derived melt and peridotite (e.g. Kelemen et al., 1998; Aulbach et al., 2002; Aulbach and Jacob, 2016), a model that is supported by the high Ni of mantle pyroxenites. A caveat with such an origin is that interaction between eclogite-derived siliceous melt and peridotite is dominated by orthopyroxene in high-P experiments under upper mantle conditions. Furthermore, the experimental reaction products have ultramafic compositions (e.g. bulk MgO > 25 wt.%; Yaxley and Green, 1998; Rapp et al., 1999; Mallik and Dasgupta, 2012, 2013), which is neither compatible with the mineralogy nor the calculated bulk composition of the Voyageur pyroxenites. The Voyageur pyroxenites would instead require interaction between a more alkaline basaltic (vs. dacitic) melt with low Si and high Ca (and Al) and peridotite in order to promote growth of clinopyroxene over orthopyroxene. Therefore, we suggest that the Voyageur pyroxenites could have crystallized within the oceanic mantle lithosphere at elevated pressures >1.5 GPa from low-degree alkaline basaltic melts, forming garnet-plagioclase-clinopyroxene assemblages (c.f. Smart et al., 2012; Foley et al., 2001), followed by fluid or melt metasomatism (e.g. Stachel et al., 2004). This origin satisfies the pyroxenite trace element compositions that seem to require crystallization of both garnet and plagioclase and supports the mantle-like oxygen isotope compositions of the pyroxenites. Attempts at trace element modeling of such assemblages from low-degree, enriched alkaline melts (e.g. basanitic), or tholeiitic melts derived from low- (e.g. MORB) and high-pressure depleted peridotite cannot faithfully produce all REE features of the pyroxenites (Fig. 11c), which is probably due to the effects of cryptic metasomatism detected in our samples (see Section 7.1 and Supplementary Fig. S1). However, although fractionated HREEs ($Yb_N/Gd_N > 2$) are produced in all three models in Fig. 11c, crystallization from basanitic alkaline liquids approaches the observed LREE enrichment of the pyroxenite xenoliths.

7.3. Structure of the Voyageur cratonic mantle and bottom-up modification

The Voyageur eclogites are distributed within the northern Slave CLM between 110 and 200 km depths, and overlap with the distribution of Voyageur peridotites (Fig. 5; Verigeanu, 2006). Five Voyageur eclogites (#361, 380A, 380B, 376 and 374) record distinct high-pressure equilibration conditions >5.5 GPa, and they correspond to depths of 180–200 km. These five eclogite xenoliths resided near the base of the estimated northern Slave lithosphere at approximately 200 km (Kopylova and Russell, 2000), and three of these "deep" eclogites (#361, 380A, 380B) also record high-temperature conditions > 1150 °C. All of the "deep" eclogites are classified as Group C (Fe^{2+}- and Ca-rich garnet), but fall into distinct trace element groups discussed above.

The Voyageur eclogites display some vertical stratification with respect to composition. With increasing eclogite equilibration pressures, garnet CaO, TiO_2, and Zr contents increase (Fig. 13); no correlation is observed between pressure and Mg-number, and FeO contents decrease with increasing pressure. Peridotites from both the Voyageur and Jericho kimberlites also display a trend of increasing fertility with depth: deeper peridotites contain garnet with higher Zr and Ti contents and olivine with lower Mg-numbers (Kopylova and Russell, 2000; Kopylova et al., 1999b; Verigeanu, 2006; Fig. 13). Vertical compositional stratification appears to be absent from Jericho eclogite xenoliths (Fig. 13). Curiously, the Voyageur CLM records a cooler thermal state (Fig. 5) than the Jericho CLM, despite the fact that the two kimberlite occurrences erupted within a 20 km radius and have similar Jurassic magma emplacement ages. However, the relatively fertile nature of both the Jericho and Voyageur peridotitic CLM, including the absence of a strongly depleted harzburgite layer (c.f. Lac de Gras CLM; Grütter et al., 1999), in combination with the pronounced vertical compositional trends discussed above, are probably related to extensive melt-related metasomatism that overprinted the northern Slave CLM (Griffin et al., 2004). In other words, the vertical compositional stratification of the Voyageur eclogite component within the northern Slave CLM may also be related to this "bottom up" metasomatic overprinting.

The source of such melt metasomatism has been ascribed to rifting accompanying the Paleoproterozoic Kilohigok Basin NE of Voyageur and Jericho (Fig. 1; Griffin et al., 2004; Grotzinger and McCormick, 1988), or to magmatism associated with the ca. 1.3 Ga Muskox intrusion and giant Mackenzie dyke swarm focused on the NW Slave craton (Davis, 1997; Heaman et al., 2006; LeCheminant and Heaman, 1989; Smart et al., 2014). Given the ~1 Gyr timescales of thermal relaxation from transient events affecting CLM (e.g. Michaut et al., 2009; Grütter, 2009; Jaupart and Mareschal, 2014), it is unlikely that Paleoproterozoic events were responsible for the thermal difference between the Jericho and Voyageur lithospheric mantle sections. However, the Mesoproterozoic Mackenzie LIP event remains a possibility. It is also possible that thermal perturbations related to either the 720 Ma Franklin LIP (Ernst et al., 2008; Heaman et al., 1992) or the widespread 680–540 Ma Laurentian kimberlite magmatism (e.g., Late Neoproterozoic kimberlites and ultramafic lamprophyres of the Coronation Gulf field on the northern Slave craton; Fig.1) (Tappe et al., 2014; 2017) are responsible for the warmer Jericho CLM by ca. 170 Ma, perhaps associated with some compositional modification. Thermal disturbances related to Jurassic kimberlite magmatic activity itself are also a possibility, but such localized transient events require longer time periods (e.g. >10–40 Myr; Grütter, 2009; Jaupart and Mareschal, 2014) to establish noticeable thermal effects on the CLM. Interestingly, while most Jericho and Voyageur eclogites have Paleoproterozoic formation ages (this study; Heaman et al., 2002; Schmidberger et al., 2005; Smart et al., 2014), ca. 1.3 Ga Nd isotope model and U-Pb zircon upper intercept ages have been obtained for Jericho eclogites (Heaman et al., 2006; Schmidberger et al., 2005). The importance of ca. 1.3 and 2.0 Ga events in having affected the northern Slave CLM is additionally supported by the Re-Os isotope systematics of Jericho peridotite xenoliths (Irvine, 2001).

In summary, the Paleoproterozoic was likely a time of widespread addition of eclogite and pyroxenite (and new peridotite?) components to the northern Slave CLM, mainly caused by collisional tectonics. Prominent CLM modification appears to be linked to the Mesoproterozoic Mackenzie LIP event, however thermal perturbations of the northern Slave CLM could also be linked to widespread Neoproterozoic-Cambrian LIP and kimberlite magmatic events.

7.4. Redox state of the mafic components in the northern Slave CLM

Peridotites from the cratonic mantle exhibit a trend of lower oxygen fugacity with increasing equilibration pressure (e.g. Creighton et al., 2009; Hanger et al., 2015; McCammon and Kopylova, 2004; Woodland and Koch, 2003; Woodland and Peltonen, 1999; Yaxley et al., 2012). This general reduction with depth is mainly a function of the increasing stability of Fe^{3+} component in garnet at higher pressures (Frost and McCammon, 2008; Rohrbach and Schmidt, 2011; Wood et al., 1990). In spite of the overall decreasing fO_2 with depth, significant heterogeneity is observed in peridotite oxidation states, which is attributable to oxidative metasomatism in the CLM (Berry et al., 2013; Creighton et al., 2009; Hanger et al., 2015; Woodland and Koch, 2003). There is a dearth of information regarding the redox state of cratonic mantle eclogite components, in part due to the long absence of an experimentally constrained eclogite oxybarometer (see Stagno et al., 2015), and the very low $Fe^{3+}/\Sigma Fe$ ratios of eclogitic garnets (e.g. Luth et al., 1990; Woodland et al., 1999). However, the few studies that do exist indicate a rough trend of relative reduction with increasing depth (Stagno et al., 2015), similar to peridotites.

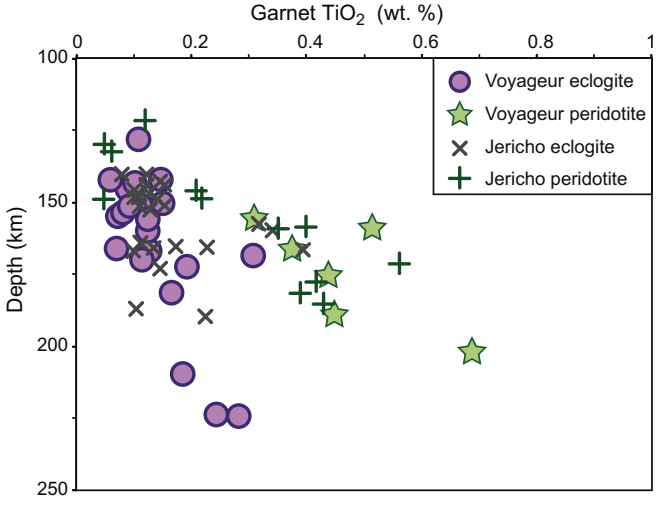

Fig. 13. Monitor of the northern Slave CLM compositional fertility with depth, as approximated by garnet TiO_2 contents with depth. Jericho and Muskox eclogite data from Smart et al. (2009, 2014); Jericho peridotite data from Kopylova et al. (1999b); Voyageur peridotite data from Verigeanu (2006).

Taken together, the subset of Voyageur samples where Fe^{3+} in garnet was measured yields a range in $\Delta \log fO_2$ of over 3 log units (Table 3). This is surprising since the majority of these samples appear to originate from a similar depth (equivalent to a pressure of ~45 kbar), straddling the graphite-diamond phase boundary (Fig. 6). However, there are differences between the sample groups. For example, the three "basaltic" eclogites (#378, #408, #370) and two gabbroic eclogites (#362A, #346) seem to follow the depth-fO_2 trend defined by Slave craton peridotites (Fig. 6; Creighton et al., 2009; McCammon and Kopylova, 2004). The altered basaltic eclogite #361, however, records significantly more oxidized conditions, even though this sample has a higher pressure of origin (P_{V06} of 68 kbar). Eclogite #361 falls within the carbonate-bearing melt stability field of Stagno et al. (2015), and we presume the relatively oxidized composition is due to oxidative metasomatism, which is consistent with the LREE-enriched composition of #361 (Fig. 9a). In contrast to the grouping of the basaltic eclogites, two of the gabbroic eclogites exhibit variable behavior. Sample #362B is significantly more reduced compared to the basaltic eclogites and the other two gabbroic eclogites found at similar depths. Gabbroic eclogite #380A equilibrated at much greater depth than the other two xenoliths, and it records more oxidizing conditions, overlapping with the metasomatised sample #361. Although this seems contrary to the expected depth-fO_2 trend described above, the presence of coarse-grained apatite in #380A indicates a more evolved bulk composition, which is corroborated by the lower Mg# for this sample compared to the other two gabbroic samples (Table 6). Thus, the higher $\Delta \log fO_2$ value may principally reflect a difference in the primary magmatic conditions under which this sample formed. Alternatively, apatite in #380A may be metasomatic in origin (e.g. Rudnick et al., 1993), and the more oxidized composition of this eclogite xenolith may result from metasomatism (e.g. Creighton et al., 2009). However, in contrast to the metasomatised eclogite #361, #380A has the lowest incompatible element content (Table 6), which does not support a significant role for metasomatic modification.

We have also calculated the fO_2 of other northern Slave eclogites using corrected garnet $Fe^{3+}/\Sigma Fe$, temperature and pressure information for Jericho and Muskox xenoliths from Kopylova et al. (2016), and our fO_2 results for these samples are shown in Fig. 6 and listed in Table 3. The Muskox and Jericho eclogites ($n = 13$) show a similar heterogeneous distribution of redox compositions as their Voyageur analogs, but the Jericho and Muskox xenoliths extend to slightly higher $\Delta \log fO_2$ values (FMQ-4.2 to −0.5 vs. FMQ-4.6 to −1.9 for Voyageur). The heterogeneous nature of the redox state of mantle eclogites, i.e. variation of fO_2 over several log units at a given depth (Fig. 6), appears to be a worldwide phenomenon (see Fig. 8 in Stagno et al., 2015), even though the database is still limited. Thus, assigning an average or common redox composition to eclogite components in the lithospheric mantle should be avoided. While the origin of the heterogeneous eclogite oxidation states remains equivocal, we suggest that the effects of seawater alteration, subduction processing and partial melting may all play a critical role (e.g. Evans, 2012; Kelley and Cottrell, 2009).

Regardless of the cause, the effect of highly variable redox gradients between eclogite/pyroxenite components and enclosing peridotite domains in Earth's upper mantle must play a key role in both redox melting proceses and metasomatic reactions, including diamond growth.

8. Conclusions

- Eclogite and pyroxenite xenoliths from the Jurassic Voyageur kimberlite in the Slave craton of northwest Canada have a large range of equilibration pressures (~40–68 kbar) and temperatures (850–1230 °C). In combination with Voyageur peridotites, it appears that the Voyageur mantle lithosphere is defined by a cooler paleogeotherm compared to the Jericho mantle section some 20 km further east on the northern Slave craton.
- Paleoproterozoic Pb model ages for clinopyroxene from the Voyageur eclogite and pyroxenite xenoliths agree with the multitude of ca. 2 Ga ages that were previously obtained for both northern and central Slave eclogites, reinforcing the importance of Paleoproterozoic modification of the Slave cratonic mantle lithosphere.
- Calculated major- and trace element bulk compositions divide the xenoliths into "basaltic" eclogites with depleted LREE but flat HREEs, and "gabbroic" eclogites with clear positive Eu anomalies and depleted HREEs. Both Voyageur eclogite groups are proposed to have protoliths within Paleoproterozoic oceanic crust.
- Voyageur pyroxenites have sinusoidal REE patterns that require a more complex origin compared to the eclogites, and we suggest that they crystallized from mafic alkaline melts in the lower reaches of Paleoproterozoic oceanic lithosphere. On the basis of our data, it can be suggested that the formation of all Voyageur eclogite and pyroxenite xenoliths is linked to subduction of oceanic lithosphere (crust and mantle) beneath the Slave craton at ca. 1.9–2 Ga during the Wopmay orogeny.
- We identified large redox heterogeneity in our Voyageur eclogite/pyroxenite xenoliths and in other eclogite xenoliths suites from the northern Slave craton (Muskox and Jericho) for which we reprocessed literature data. Over a similar depth interval, the eclogites show an extraordinarily large range of ~3 log units of oxygen fugacity, and there exist no relationships between fO_2 and depth of equilibration for the northern Slave cratonic eclogite component. Stark redox contrasts between mafic and peridotitic lithologies within continental roots, as demonstrated for the northern Slave craton, are likely among the key drivers of volatile mobility and associated melting reactions in Earth's upper mantle.

Supplementary data to this article can be found online at http://dx.doi.org/10.1016/j.chemgeo.2016.10.014.

Acknowledgement

We gratefully acknowledge De Beers Canada Inc. for collection and provision of the research samples from Voyageur. Sergei Matveev is thanked for his assistance with microprobe analysis in Alberta. We thank Dirk Frei for his assistance with LA-ICP-MS analysis at CAF (Stellenbosch University). Tom Chacko, Thomas Stachel, and Larry Heaman are kindly thanked for their support during initial project planning. KAS acknowledges a Claude Leon Foundation research award, and ST was a Humboldt Foundation (Feodor Lynen program) scholar at the University of Alberta during inception of the project. KAS and ST acknowledge support from the CIMERA DST-NRF Centre of Excellence at the University of Johannesburg. We thank the journal reviewers Sonja Aulbach and Sami Mikhail, and guest-editor Alex McCoy-West for their thorough and thoughtful comments.

References

Alt, J.C., Teagle, D.A.H., 2000. Hydrothermal alteration and fluid fluxes in ophiolites and oceanic crust. In: Dilek, Y., Moores, E., Elthon, D., Nicolas, A. (Eds.), Geol. Soc. Am. Spec. Paper 349, Ophiolites and Oceanic Crust: New Insights From Field Studies and Ocean Drilling Program, pp. 273–282.
Alt, J.C., Muehlenbachs, K., Honnorez, J., 1986. An oxygen isotopic profile through the upper kilometer of the oceanic crust, DSDP Hole 504B. Earth Planet. Sci. Lett. 80, 217–229.
Aulbach, S., 2012. Craton nucleation and formation of thick lithospheric roots. Lithos 1–15.
Aulbach, S., Jacob, D.E., 2016. Major- and trace-elements in cratonic mantle eclogites and pyroxenites reveal heterogeneous sources and metamorphic processing of low-pressure protoliths. Lithos 262, 586–605.
Aulbach, S., Viljoen, K.S., 2015. Eclogite xenoliths from the Lace kimberlite, Kaapvaal craton: from convecting mantle source to palaeo-ocean floor and back. Earth Planet. Sci. Lett. 431, 274–286 9.
Aulbach, S., Stachel, T., Viljoen, S.K., Brey, G.P., Harris, J.W., 2002. Eclogitic and websteritic diamond sources beneath the Limpopo Belt – is slab-melting the link? Contrib. Mineral. Petrol. 143, 56–70.
Aulbach, S., Pearson, N.J., O'Reilly, S.Y., Doyle, B.J., 2007. Origins of xenolithic eclogites and pyroxenites from the Central Slave Craton, Canada. J. Petrol. 48, 1843–1873.
Aulbach, S., Creaser, R.A., Pearson, N.J., Simonetti, S.S., Heaman, L.M., Griffin, W.L., Stachel, T., 2009a. Sulfide and whole rock Re–Os systematics of eclogite and pyroxenite xenoliths from the Slave Craton, Canada. Earth Planet. Sci. Lett. 283, 48–58.
Aulbach, S., Stachel, T., Creaser, R.A., Heaman, L.M., Shirey, S.B., Muehlenbachs, K., Eichenberg, D., Harris, J.W., 2009b. Sulphide survival and diamond genesis during formation and evolution of Archaean subcontinental lithosphere: a comparison between the Slave and Kaapvaal cratons. Lithos 112, 747–757.
Aulbach, S., Stachel, T., Heaman, L.M., Carlson, J.A., 2011. Microxenoliths from the Slave craton: archives of diamond formation along fluid conduits. Lithos 126, 419–434.
Aulbach, S., Gerdes, A., Viljoen, K.S., 2016. Formation of diamondiferous kyanite–eclogite in a subduction mélange. Geochim. Cosmochim. Acta 179, 156–176.
Bach, W., Alt, J.C., Niu, Y., Humphris, S.E., Erzinger, J., Dick, H., 2001. The geochemical consequences of late-stage low-grade alteration of lower ocean crust at the SW Indian Ridge: results from ODP Hole 735B (Leg 176). Geochim. Cosmochim. Acta 65, 3267–3287.
Baker, J., Peate, D., Waight, T., MeyzeN, C., 2004. Pb isotopic analysis of standards and samples using a Pb-Pb double spike and thallium to correct for mass bias with a double-focusing MC-ICP-MS. Chem. Geol. 211, 275–303.
Barth, M.G., Rudnick, R.L., Horn, I., McDonough, W.F., Spicuzza, M.J., Valley, J.W., Haggerty, S.E., 2001. Geochemistry of xenolithic eclogites from West Africa, part I: a link between low MgO eclogites and Archean crust formation. Geochim. Cosmochim. Acta 65, 1499–1527.
Barth, M.G., Foley, S.F., Horn, I., 2002b. Partial melting in Archean subduction zones: constrains from experimentally determined trace element partition coefficients between eclogitic minerals and tonalitic melts under upper mantle conditions. Precambrian Res. 113, 323–340.
Benoit, M., Polvé, M., Ceuleneer, G., 1996. Trace element and isotopic characterization of mafic cumulates in a fossil mantle diapir (Oman ophiolite). Chem. Geol. 134, 199–214.
Berry, A.J., Yaxley, G.M., Hanger, B.J., Woodland, A.B., de Jonge, M.D., Howard, D.L., Paterson, D., Kamenetsky, V.S., 2013. Quantitative mapping of the oxidative effects of mantle metasomatism. Geology 41, 683–686.
Beyer, C., Frost, D.J., Miyajima, N., 2015. Experimental calibration of a garnet–clinopyroxene geobarometer for mantle eclogites. Contrib. Mineral. Petrol. 169, 18.
Bindeman, I.L., Davis, A.M., 2000. Trace element partitioning between plagioclase and melt: Investigation of dopant influence on partition behavior. Geochim. Cosmochim. Acta. 64, 2863–2878.
Bleeker, W., Hall, B., 2007. The slave craton: geological and metallogenic evolution. In: Goodfellow, W.D. (Ed.), Mineral Deposits of Canada: A Synthesis of Major Deposit-types, District Metallogeny, the Evolution of Geological Provinces, and Exploration Methods: Geologic Association of Canada. Mineral Deposits Division, Special Publication, Geological Association of Canada, pp. 849–879.
Bleeker, W., Ketchum, J.W., Davis, W.J., 1999. The Central Slave Basement Complex, part II: age and tectonic significance of high-strain zones along the basement–cover contact. Can. J. Earth Sci. 36, 111–1130.
Bodinier, J.-L., Godard, M., 2003. Orogenic, ophiolitic, and abyssal peridotites. Treat. Geochem. 2, 103–170.
Buchan, K.L., LeCheminant, A.N., van Breemen, O., 2009. Paleomagnetism and U–Pb geochronology of the Lac de Gras diabase dyke swarm, Slave Province, Canada: implications for relative drift of Slave and Superior provinces in the Paleoproterozoic. Can. J. Earth Sci. 46, 361–379.
Chen, W., Simonetti, A., 2015. Isotopic (Pb, Sr, Nd, C, O) evidence for plume-related sampling of an ancient, depleted mantle reservoir. Lithos 216–217, 81–92.
Cherniak, D.J., 2001. Pb diffusion in Cr diopside, augite, and enstatite, and consideration of the dependence of cation diffusion in pyroxene on oxygen fugacity. Chem. Geol. 177, 381–397.
Coleman, R.G., Lee, D.E., Beatty, L.B., Brannock, W.W., 1965. Eclogites and eclogites: their differences and similarities. Geol. Soc. Am. Bull. 483–508.
Cook, F.A., van der Velden, A.J., Hall, K.W., 1999. Frozen subduction in Canada's Northwest Territories: lithoprobe deep lithospheric reflection profiling of the western Canadian Shield. Tectonics 18, 1–24.
Creaser, R.A., Grütter, H., Carlson, J., Crawford, B., 2004. Macrocrystal phlogopite Rb–Sr dates for the Ekati property kimberlites, Slave Province, Canada: evidence for multiple intrusive episodes in the Paleocene and Eocene. Lithos 76, 399–414.
Creighton, S., Stachel, T., Eichenberg, D., Luth, R.W., 2009. Oxidation state of the lithospheric mantle beneath Diavik diamond mine, central Slave craton, NWT, Canada. Contrib. Mineral. Petrol. 159, 645–657.

Davis, W.J., 1997. U-Pb zircon and rutile ages from granulite xenoliths in the Slave province: evidence for mafic magmatism in the lower crust. Geology 25, 343–346.
Davis, W., Jones, A.G., Bleeker, W., Grütter, H., 2003. Lithosphere development in the Slave craton: a linked crustal and mantle perspective. Lithos 71, 575–589.
De Stefano, A., Kopylova, M.G., Cartigny, P., Afanasiev, V., 2009. Diamonds and eclogites of the Jericho kimberlite (Northern Canada). Contrib. Mineral. Petrol. 158, 295–315.
Dongre, A.N., Jacob, D.E., Stern, R.A., 2015. Subduction-related origin of eclogite xenoliths from the Wajrakarur kimberlite field, Eastern Dharwar craton, Southern India: constraints from petrology and geochemistry. Geochim. Cosmochim. Acta 166, 165–188.
Eiler, J.M., 2001. Oxygen isotope variations of basaltic lavas and upper mantle rocks. Rev. Mineral. Geochem. 43, 320–364.
Eiler, J., Stolper, E.M., McCanta, M.C., 2011. Intra- and Intercrystalline oxygen isotope variations in minerals from basalts and peridotites. J. Petrol. 52, 1393–1413.
Ellis, D.J., Green, D.H., 1979. An experimental study of the effect of Ca upon garnet-clinopyroxene Fe-Mg exchange equilibria. Contrib. Mineral. Petrol. 71, 13–22.
Ernst, R.E., Wingate, M.T.D., Buchan, K.L., Li, Z.X., 2008. Global record of 1600–700 Ma Large Igneous Provinces (LIPs): implications for the reconstruction of the proposed Nuna (Columbia) and Rodinia supercontinents. Precambrian Res. 160, 159–178.
Evans, K.A., 2012. Earth-science reviews. Earth Sci. Rev. 113, 11–32.
Foley, S.F., Petibon, C.M., Jenner, G.A., Kjarsgaard, B.A., 2001. High U/Th partitioning by clinopyroxene from alkali silicate and carbonatite metasomatism: an origin for Th/U disequilibrium in mantle melts? Terra Nova 13, 104–109.
Frost, D.J., McCammon, C.A., 2008. The redox state of Earth's mantle. Annu. Rev. Earth Planet. Sci. 36, 389–420.
Gale, A., Dalton, C.A., Langmuir, C.H., Su, Y.J., Schilling, J.G., 2013. The mean composition of ocean ridge basalts. Geochem. Geophys. Geosyst. 14, 489–518.
Garrido, C.J., Bodinier, J.-L., Burg, J.-P., Zeilinger, G., Hussain, S.S., Dawood, H., Chaudhry, M.N., Gervilla, F., 2006. Petrogenesis of mafic garnet granulite in the lower crust of the Kohistan paleo-arc complex (Northern Pakistan): implications for intra-crustal differentiation of island arcs and generation of continental crust. J. Petrol. 47, 1873–1914.
Greau, Y., Huang, J.-X., Griffin, W.L., Renac, C., Alard, O., O'Reilly, S.Y., 2011. Type I eclogites from Roberts Victor kimberlites: products of extensive mantle metasomatism. Geochim. Cosmochim. Acta 75, 6927–6954.
Green, D.H., Ringwood, A.E., 1967. The genesis of basaltic magmas. Contrib. Mineral. Petrol. 15, 103–190.
Green, T.H., Blundy, J.D., Adam, J., Yaxley, G.M., 2000. SIMS determination of trace element partition coefficients between garnet, clinopyroxene and hydrous basaltic liquids at 2–7.5 GPa and 1080–1200. Lithos 165–187.
Griffin, W.L., O'Reilly, S.Y., 2007. Cratonic lithospheric mantle: is anything subducted? Episodes 30, 43.
Griffin, W.L., Doyle, B.J., Ryan, C.G., Pearson, N.J., O'Reilly, S.Y., Natapov, L., Kivi, K., Kretschmar, U., Ward, J., 1999. Lithospheric structure and mantle terranes: Slave craton, Canada. In: Gurney, J.J., Gurney, J.L., Pascoe, M.D., Richardson, S.H. (Eds.), The J.B. Dawson Volume: Proceedings of the VIIth Inernational Kimberlite Conference, pp. 299–306.
Griffin, W.L., O'Reilly, S.Y., Abe, N., Aulbach, S., Davies, R.M., Pearson, N.J., Doyle, B.J., Kivi, K., 2003. The origin and evolution of Archean lithospheric mantle. Precambrian Res. 127, 19–41.
Griffin, W.L., O'Reilly, S.Y., Doyle, B.J., Pearson, N.J., Coopersmith, H., Kivi, K., Malkovets, V., Pokhilenko, N., 2004. Lithosphere mapping beneath the North American plate. Lithos 77, 873–922.
Grotzinger, J.P., McCormick, D.S., 1988. Flexure of the early Proterozoic lithosphere and evolution of Kilohigok Basin (1.9 Ga), northwest Canadian Shield. In: Kleinspehn, K.L., et al. (Eds.), New Perspectives in Basin Analysis. Springer-Verlag, New York Inc., pp. 405–430.
Grütter, H.S., 2009. Pyroxene xenocryst geotherms: techniques and application. Lithos 112S, 1167–1178.
Grütter, H.S., Apter, D.B., Kong, J., 1999. Crust-mantle coupling: evidence from mantle-derived xenocrystic garnets. In: Gurney, J.J., Gurney, J.L., Pascoe, M.D., Richardson, S.H. (Eds.), Presented at the the J.B. Dawson Volume: Proceedings of the VIIth Inernational Kimberlite Conference, pp. 307–313.
Gurney, J.J., Helmstaedt, H.H., Richardson, S.H., Shirey, S.B., 2010. Diamonds through time. Econ. Geol. 105, 689–712.
Gysi, A.P., Jagoutz, O., Schmidt, M.W., Targuisti, K., 2011. Petrogenesis of pyroxenites and melt infiltrations in the ultramafic complex of Beni Bousera, Northern Morocco. J. Petrol. 52, 1679–1735.
Hanger, B.J., Yaxley, G.M., Berry, A.J., Kamenetsky, V.S., 2015. Relationships between oxygen fugacity and metasomatism in the Kaapvaal subcratonic mantle, represented by garnet peridotite xenoliths in the Wesselton kimberlite, South Africa. Lithos 212–215, 443–452.
Harris, C., Vogeli, J., 2010. Oxygen isotope composition of garnet in the Peninsula Granite, Cape Granite Suite, South Africa: constrains on melting and emplacement mechanisms. S. Afr. J. Geol. 113, 401–412.
Hart, S.R., Blusztain, J., Dick, H.J.B., Meyer, P.S., Muehlenbachs, K., 1999. The fingerprint of seawater circulation in a 500-meter section of ocean crust gabbros. Geochim. Cosmochim. Acta 23 (24), 4059–4080.
Heaman, L.M., LeCheminant, A.N., Rainbird, R.H., 1992. Nature and timing of Franklin igneous events, Canada: implications for Late Protereozoic mantle plume and the break-up of Laurentia. Earth Planet. Sci. Lett. 109, 116–131.
Heaman, L.M., Creaser, R.A., Cookenboo, H.O., 2002. Extreme enrichment of high field strength elements in Jericho eclogite xenoliths: a cryptic record of Paleoproterozoic subduction, partial melting, and metasomatism beneath the Slave craton, Canada. Geology 30, 507–510.
Heaman, L.M., Kjarsgaard, B.A., Creaser, R.A., 2003. The timing of kimberlite magmatism in North America: implications for global kimberlite genesis and diamond exploration. Lithos 71, 153–184.
Heaman, L.M., Creaser, R.A., Cookenboo, H., Chacko, T., 2006. Multi-stage modification of the northern slave mantle lithosphere: evidence from zircon- and diamond-bearing eclogite xenoliths entrained in Jericho Kimberlite, Canada. J. Petrol. 47, 821–858.
Helmstaedt, H., 2009. Crust–mantle coupling revisited: the Archean Slave craton, NWT, Canada. Lithos 112, 1055–1068.
Helmstaedt, H.H., Doig, R., 1975. Eclogite nodules from kimberlite pipes of the Colorado plateau-samples of subducted Franciscan-type oceanic lithosphere. Phys. Chem. Earth 9, 95–111.
Hildebrand, R.S., Hoffmann, P.F., Bowring, S.A., 1987. Tectono-magmatic evolution of the 1.9-Ga Great Bear magmatic zone, Wopmay Orogen, Northwestern Canada. J. Volcanol. Geotherm. Res. 32, 99–118.
Hoffmann, P.F., 1989. Precambrian geology and tectonic history of North America. In: Bally, A.W., Palmer, A.R. (Eds.), The Geology of North America: An Overview. Geological Society of America, pp. 447–512.
Huang, J.-X., Greau, Y., Griffin, W.L., O'Reilly, S.Y., Pearson, N.J., 2012. Multi-stage origin of Roberts Victor eclogites: progressive metasomatism and its isotopic effects. Lithos 142–143, 161–181.
Hunt, L., T S., Grutter, H., Armstrong, J., McCandless, T.E., Simonetti, A., Tappe, S., 2012. Small mantle fragments from the Renard Kimberlites, Quebec: powerful recorders of mantle lithosphere formation and modification beneath the eastern Superior craton. J. Petrol. 53, 1597–1635.
Ireland, T.R., Rudnick, R.L., Spetsius, Z., 1994. Trace elements in diamond inclusions from eclogites reveal link to Archean granites. Earth Planet. Sci. Lett. 128, 199–213.
Irvine, G.J., 2001. Time Constraints on the Formation of Lithospheric Mantle Beneath Cratons: A Re-Os Isotope and Platinum Group Element Study of Peridotite Xenoliths From Northern Canada and Lesotho. Durham University.
Jacob, D.E., 2004. Nature and origin of eclogite xenoliths from kimberlites. Lithos 77, 295–316.
Jacob, D.E., Foley, S.F., 1999. Evidence for Archean ocean crust with low high field strength element signature from diamondiferous eclogite xenoliths. Lithos 48, 317–336.
Jacob, D., Jagoutz, E., Lowry, D., Mattey, D., Kudrjavtseva, G., 1994. Diamondiferous eclogites from Siberia: remnants of Archean oceanic crust. Geochim. Cosmochim. Acta 58, 5191–5207.
Jacob, D.E., Bizimis, M., Salters, V.J.M., 2005. Lu-Hf and geochemical systematics of recycled ancient oceanic crust: evidence from Roberts Victor eclogites. Contrib. Mineral. Petrol. 148, 707–720.
Jacob, D.E., Viljoen, K.S., Grassineau, N.V., 2009. Eclogite xenoliths from Kimberley, South Africa — a case study of mantle metasomatism in eclogites. Lithos 112, 1002–1013.
Jagoutz, E., Dawson, J.B., Hoernes, S., Spettel, B., Waenke, H., 1985. Anorthositic Oceanic Crust in the Archean Earth 1. pp. 40–41.
Jaupart, C., Mareschal, J.-C., 2014. 4.2 constraints on crustal heat production from heat flow data. In: Holland, H., Turekian, K. (Eds.), Treatise on Geochemistry. Elsevier Ltd, pp. 53–73.
Jenner, F.E., O'Neill, H.S.C., 2012. Analysis of 60 elements in 616 ocean floor basaltic glasses. Geochem. Geophys. Geosyst. 13, 1–11.
Jerde, E.A., Taylor, L.A., Crozaz, G., Sobolev, N.V., Sobolev, V.N., 1993. Diamondiferous eclogites from Yakutia, Siberia: evidence for a diversity of protoliths. Contrib. Mineral. Petrol. 114, 189–202.
Kelemen, P.B., Hart, S.R., Bernstein, S., 1998. Silica enrichment in the continental upper mantle via melt/rock reaction. Earth Planet. Sci. Lett. 164, 387–406.
Kelley, K.A., Cottrell, E., 2009. Water and the oxidation state of subduction zone magmas. Science 325, 605–607.
Kennedy, C.S., Kennedy, G.C., 1976. The equilibrium boundary between graphite and diamond. J. Geophys. Res. Solid Earth 81, 2467–2470 (1978–2012).
Klemme, S., Blundy, J.D., Wood, B.J., 2002. Experimental constraints on major and trace element partitioning during partial melting of eclogite. Geochim. Cosmochim. Acta 66, 3109–3123.
Koepke, J., Feig, S.T., Snow, J., Freise, M., 2004. Petrogenesis of oceanic plagiogranites by partial melting of gabbros: an experimental study. Contrib. Mineral. Petrol. 146, 414–432.
Koepke, J., Berndt, J., Horn, I., Fahle, J., Wolff, P.E., 2014. Partial melting of oceanic gabbro triggered by migrating water-rich fluids: a prime example from the Oman Ophiolite. Geol. Soc. Lond., Spec. Publ. 392, 195–212.
Kopylova, M.G., Russell, J.K., 2000. Chemical stratification of cratonic lithosphere: constraints from the Northern Slave craton, Canada. Earth Planet. Sci. Lett. 181, 71–87.
Kopylova, M.G., Russell, J.K., Cookenboo, H., 1999a. Mapping the lithosphere beneath the North Central Slave Craton. In: Gurney, J.J., Gurney, J.L., Pascoe, M.D., Richardson, S.H. (Eds.), Presented at the the J.B. Dawson Volume: Proceedings of the VIIth Inernational Kimberlite Conference, Cape Town, pp. 468–479.
Kopylova, M.G., Russell, J.K., Cookenboo, H., 1999b. Petrology of peridotite and pyroxenite xenoliths from the Jericho Kimberlite: implications for the thermal state of the mantle beneath the Slave Craton, Northern Canada. J. Petrol. 40, 79–104.
Kopylova, M.G., Beausoleil, Y., Goncharov, A., Burgess, J., Strand, P., 2016. Spatial distribution of eclogite in the Slave cratonic mantle: the role of subduction. Tectonophysics 672-673, 87–103.
LeCheminant, A.N., Heaman, L.M., 1989. Mackenzie igneous events, Canada: Middle Proterozoic hotspot magmatism associated with ocean opening. Earth Planet. Sci. Lett. 96, 38–48.
Lee, C.-T.A., Luffi, P., Chin, E.J., 2011. Building and destroying continental mantle. Annu. Rev. Earth Planet. Sci. 39, 59–90.
Luth, R.W., Virgo, D., Boyd, F.R., Wood, B.J., 1990. Ferric iron in mantle-derived garnets. Contrib. Mineral. Petrol. 104, 56–72.
MacGregor, I.D., Manton, W.I., 1986. Roberts Victor eclogites: ancient oceanic crust. J. Geophys. Res. Solid Earth 91, 14063–14079 (1978–2012).
Mallik, A., Dasgupta, R., 2012. Reaction between MORB-eclogite derived melts and fertile peridotite and generation of ocean island basalts. Earth Planet. Sci. Lett. 329–330, 97–108.

Mallik, A., Dasgupta, R., 2013. Reactive infiltration of MORB-eclogite-derived carbonated silicate melt into fertile peridotite at 3 GPa and genesis of alkali magmas. J. Petrol. 54, 2267–2300.
Mattey, D., Lowry, D., Macpherson, C., 1994. Oxygen isotope composition of mantle peridotite. Earth Planet. Sci. Lett. 128, 231–241.
McCammon, C., Kopylova, M.G., 2004. A redox profile of the Slave mantle and oxygen fugacity control in the cratonic mantle. Contrib. Mineral. Petrol. 148, 55–68.
McCoy-West, A.J., Bennet, V.C., Amelin, Y., 2016. Rapid Cenozoic ingrowth of isotopic signatures simulating "HIMU" in ancient lithospheric mantle: distinguishing source from process. Geochim. Cosmochim. Acta 187, 79–101.
McDonough, W.F., Sun, S.S., 1995. The composition of the Earth. Chem. Geol. 120, 223–253.
Menzies, M.A., Fan, W., Zhang, M., 1993. Palaeozoic and Cenozoic lithoprobes and the loss of >120 km of Archaean lithosphere, Sino-Korean craton, China. Geol. Soc. Lond., Spec. Publ. 76, 71–81.
Menzies, A.H., Carlson, R.W., Shirey, S.B., Gurney, J.J., 2003. Re–Os systematics of diamond-bearing eclogites from the Newlands kimberlite. Lithos 71, 323–336.
Michaut, C., Jaupart, C., Mareschal, J.C., 2009. Thermal evolution of cratonic roots. Lithos 109, 47–60.
Monnier, C., Girardeau, J., Permana, H., Rehault, J.-P., Bellon, H., Cotten, J., 2003. Dynamics and age of formation of the Seram-Ambon ophiolites (Central Indonesia). Bull. Soc. Geol. Fr. 174, 529–543.
Nimis, P., Taylor, W.R., 2000. Single clinopyroxene thermobarometry for garnet peridotites. Part I. Calibration and testing of a Cr-in-clinopyroxene barometerand an enstatite-in-clinopyroxene thermometer. Contrib. Mineral. Petrol. 139, 541–554.
Norman, M., Garcia, M.O., Pietruszka, A.J., 2005. Trace-element distribution coefficients for pyroxenes, plagioclase, and olivine in evolved tholeiites from the 1955 eruption of Kilauea Volcano, Hawai'i, and petrogenesis of differentiated rift-zone lavas. Am. Mineral. 90, 888–899.
O'Reilly, S.Y., Griffin, W.L., 2000. Apatite in the mantle: implications for metasomatic processes and high heat production in Phanerozoic mantle. Lithos 53, 217–232.
Pearce, N., Perkins, W.T., Westgate, J.A., 1997. A compilation of new and published major and trace element data for NIST SRM 610 and NIST SRM 612 glass reference materials. Geostand. Newslett. 21, 115–144.
Pearson, D.G., 1999. The age of continental roots. Lithos 48, 171–194.
Pearson, D.G., Wittig, N., 2008. Formation of Archaean continental lithosphere and its diamonds: the root of the problem. J. Geol. Soc. 165, 895–914.
Pearson, D.G., Wittig, N., 2014. 3.6 the formation and evolution of cratonic mantle lithosphere – evidence from mantle xenoliths. In: Carlson, R.W. (Ed.), Treatise on Geochemistry, 2nd ed. Elsevier Ltd., pp. 255–292.
Pearson, D.G., Davies, G.R., Nixon, P.H., 1993. Geochemical constraints on the petrogenesis of diamond facies pyroxenites from the Beni Bousera Peridotite Massif, North Morocco. J. Petrol. 34, 125–172.
Pearson, D.G., Canil, D., Shirey, S.B., 2014. 3.5 mantle samples included in volcanic rocks: xenoliths and diamonds. In: Carlson, R.W. (Ed.), Treatise on Geochemistry, 2nd ed. Elsevier Ltd., pp. 169–253.
Peltonen, P., Kontinen, A., Huhma, H., 1998. Petrogenesis of the mantle sequence of the Jormua Ophiolite (Finland): melt migration in the upper mantle during palaeoproterozoic continental break-up. J. Petrol. 39, 297–329.
Pernet-Fisher, J.F., Howarth, G.H., Liu, Y., Barry, P.H., Carmody, L., Valley, J.W., Bodnar, R.J., Spetsius, Z.V., Taylor, L.A., 2014. Komsomolskaya diamondiferous eclogites: evidence for oceanic crustal protoliths. Contrib. Mineral. Petrol. 167, 981.
Rapp, R.P., Shimizu, N., Norman, M.D., Applegate, G.S., 1999. Reaction between slab-derived melts and peridotite in the mantle wedge: experimental constraints at 3.8 GPa. Chem. Geol. 160, 335–356.
Richardson, S.H., Shirey, S.B., Harris, J.W., Carlson, R.W., 2001. Archean subduction recorded by Re–Os isotopes in eclogitic sulfide inclusions in Kimberley diamonds. Earth Planet. Sci. Lett. 191, 257–266.
Richardson, S.H., Shirey, S.B., Harris, J.W., 2004. Episodic diamond genesis at Jwaneng, Botswana, and implications for Kaapvaal craton evolution. Lithos 77, 143–154.
Riches, A.J.V., Liu, Y., Day, J.M.D., Spetius, Z.V., Taylor, L.A., 2010. Subducted oceanic crust as diamond hosts revealed by garnets of mantle xenoliths from Nyurbinskaya, Siberia. Lithos 120, 368–378 d.
Riches, A.J.V., Ickert, R.B., G, P.D., Stern, R.A., Jackson, S.E., Ishikawa, A., Kjarsgaard, B.A., Gurney, J.J., 2016. In situ oxygen-isotope, major-, and trace-element constraints on the metasomatic modification and crustal origin of a diamondiferous eclogite from Roberts Victor, Kaapvaal Craton. Geochim. Cosmochim. Acta 174, 345–359.
Rohrbach, A., Schmidt, M.W., 2011. Redox freezing and melting in the Earth's deep mantle resulting from carbon–iron redox coupling. Nature 472, 209–212.
Rudnick, R.L., McDonough, W.F., Chappell, B.W., 1993. Carbonatite metasomatism in the northern Tanzanian mantle: petrographic and geochemical characteristics. Earth Planet. Sci. Lett. 114, 463–475.
Schmickler, B., Jacob, D.E., Foley, S.F., 2004. Eclogite xenoliths from the Kuruman kimberlites, South Africa: geochemical fingerprinting of deep subduction and cumulate processes. Lithos 75, 173–207.
Schmidberger, S.S., Francis, D., 2001. Constraints on the trace element composition of the Archean mantle root beneath Somerset Island, Arctic Canada. J. Petrol.
Schmidberger, S.S., Heaman, L.M., Simonetti, A., Creaser, R.A., Cookenboo, H., 2005. Formation of Paleoproterozoic eclogitic mantle, Slave Province (Canada): insights from in-situ Hf and U–Pb isotopic analyses of mantle zircons. Earth Planet. Sci. Lett. 240, 621–633.
Schmidberger, S.S., Simonetti, A., Heaman, L.M., Creaser, R.A., Whiteford, S., 2007. Lu–Hf, in-situ Sr and Pb isotope and trace element systematics for mantle eclogites from the Diavik diamond mine: evidence for Paleoproterozoic subduction beneath the Slave craton, Canada. Earth Planet. Sci. Lett. 254, 55–68.
Schmidt, M.W., Poli, S., 2014. 4.9 devolatilization during subduction. In: Holland, H., Turekian, K. (Eds.), Treatise on Geochemistry, 2nd ed. Elsevier Ltd, pp. 669–701.
Schulze, D.J., Valley, J.W., Spicuzza, M.J., 2000. Coesite eclogites from the Roberts Victor kimberlite, South Africa. Lithos 54, 23–32.
Shirey, S.B., Richardson, S.H., 2011. Start of the Wilson cycle at 3 Ga shown by diamonds from subcontinental mantle. Science 333, 434–436.
Shirey, S.B., Harris, J.W., Richardson, S.H., Fouch, M.J., James, D.E., Cartigny, P., Deines, P., Viljoen, F., 2002. Diamond genesis, seismic structure, and evolution of the Kaapvaal-Zimbabwe craton. Science 297, 1683–1686.
Shirey, S.B., Richardson, S.H., Harris, J.W., 2004. Integrated models of diamond formation and craton evolution. Lithos 77, 923–944.
Smart, K.A., Heaman, L.M., Chacko, T., Simonetti, A., Kopylova, M., Mah, D., Daniels, D., 2009. The origin of high-MgO diamond eclogites from the Jericho Kimberlite, Canada. Earth Planet. Sci. Lett. 284, 527–537.
Smart, K.A., Chacko, T., Stachel, T., Muehlenbachs, K., Stern, R.A., Heaman, L.M., 2011. Diamond growth from oxidized carbon sources beneath the Northern Slave Craton, Canada: a δ13C–N study of eclogite-hosted diamonds from the Jericho kimberlite. Geochim. Cosmochim. Acta 75, 6027–6047.
Smart, K.A., Chacko, T., Stachel, T., Tappe, S., Stern, R.A., Ickert, R.B., EIMF, 2012. Eclogite formation beneath the northern Slave craton constrained by diamond inclusions: oceanic lithosphere origin without a crustal signature. Earth Planet. Sci. Lett. 319-320, 165–177.
Smart, K.A., Chacko, T., Simonetti, A., Sharp, Z.D., Heaman, L.M., 2014. A record of paleoproterozoic subduction preserved in the Northern Slave Cratonic Mantle: Sr-Pb-O isotope and trace-element investigations of eclogite xenoliths from the Jericho and Muskox Kimberlites. J. Petrol. 55, 549–583.
Smyth, J.R., Caporuscio, F.A., McCormick, T.C., 1989. Mantle eclogites: evidence of igneous fractionation in the mantle. Earth Planet. Sci. Lett. 93, 133–141.
Stacey, J.S., Kramers, J.D., 1975. Approximation of terrestrial lead isotope evolution by a two-stage model. Earth Planet. Sci. Lett. 26, 207–221.
Stachel, T., Aulbach, S., Brey, G.P., Harris, J.W., Leost, I., Viljoen, K.S., 2004. The trace element composition of silicate inclusions in diamonds: a review. Lithos 77, 1–19.
Stagno, V., Frost, D.J., McCammon, C.A., Mohseni, H., Fei, Y., 2015. The oxygen fugacity at which graphite or diamond forms from carbonate-bearing melts in eclogitic rocks. Contrib. Mineral. Petrol. 169, 16.
Stracke, A., Bizimis, M., Salters, V.J.M., 2003. Recycling oceanic crust: quantitative constraints. Geochem. Geophys. Geosyst. 4, 1525–2027.
Tappe, S., Foley, S.F., Stracke, A., Romer, R.L., Kjarsgaard, B.A., Heaman, L.M., Joyce, N., 2007. Craton reactivation on the Labrador Sea margins: $^{40}Ar/^{39}Ar$ age and Sr–Nd–Hf–Pb isotope constraints from alkaline and carbonatite intrusives. Earth Planet. Sci. Lett. 256, 433–454.
Tappe, S., Smart, K.A., Pearson, D.G., Steenfelt, A., Simonetti, A., 2011. Craton formation in Late Archean subduction zones revealed by first Greenland eclogites. Geology 39, 1103–1106.
Tappe, S., Pearson, D.G., Kjarsgaard, B.A., Nowell, G., Dowall, D., 2013. Mantle transition zone input to kimberlite magmatism near a subduction zone: origin of anomalous Nd-Hf isotope systematics at Lac de Gras, Canada. Earth Planet. Sci. Lett. 371-372, 235–251.
Tappe, S., Kjarsgaard, B.A., Kurszlaukis, S., Nowell, G.M., Phillips, D., 2014. Petrology and Nd-Hf isotope geochemistry of the Neoproterozoic Amon kimberlite sills, Baffin Island (Canada): evidence for deep mantle magmatic activity linked to supercontinent cycles. J. Petrol. 55, 2003–2042.
Tappe, S., Brand, N.B., Stracke, A., van Acken, D., Liu, C.-Z., Strauss, H., Wu, F.-Y., Luguet, A., Mitchell, R.H., 2017. Plates or plumes in the origin of kimberlites: U/Pb perovskite and Sr-Nd-Hf-Os-C-O isotope constraints from the Superior craton (Canada). Chem. Geol. 455, 52–78.
Tappe, S., Smart, K.A., Stracke, A., Romer, R.L., Prelevic, D., van den Bogaard, P., 2016. Melt evolution beneath a rifted craton edge: $^{40}Ar/^{39}Ar$ geochronology and Sr–Nd–Hf–Pb isotope systematics of primitive alkaline basalts and lamprophyres from the SW Baltic Shield. Geochim. Cosmochim. Acta 173, 1–36.
Taylor, W.R., 1998. An experimental test of some geothermometer and geobarometer formulations for upper mantle peridotites with application to the thermobarometry of fertile lherzolite and garnet websterite. N. Jb. Miner. Abh. 172, 381–408.
Taylor, L.A., Neal, C.R., 1989. Eclogites with oceanic crustal and mantle signatures from the Bellsbank kimberlite, South Africa, part I: mineralogy, petrography, and whole rock chemistry. J. Geol. 551–567.
Van Achterbergh, E., Ryan, C.G., Jackson, S.E., Griffin, W.L., 2001. Data reduction software for LA-ICP-MS. In: Sylvester, P. (Ed.), Laser-Ablation-ICPMS in the Earth Sciences. Mineralogical Association of Canada, Short Courses, pp. 239–243.
Verigeanu, E.D., 2006. A Study of Peridotite Xenoliths From the Voyageur Kimberlite, Slave Craton, Canada. University of Alberta, Edmonton.
Westerlund, K.J., Shirey, S.B., Richardson, S.H., Carlson, R.W., Gurney, J.J., Harris, J.W., 2006. A subduction wedge origin for Paleoarchean peridotitic diamonds and harzburgites from the Panda kimberlite, Slave craton, evidence from Re-Os isotope systematics. Contrib. Mineral. Petrol. 152, 275–294.
White, W.M., 1993. $^{238}U/^{204}Pb$ in MORB and open system evolution of the depleted mantle. Earth Planet. Sci. Lett. 115, 211–226.
Williams, H.M., Nielsen, S.G., Renac, C., Griffin, W.L., O'Reilly, S.Y., McCammon, C.A., Pearson, N., Viljoen, F., Alt, J.C., Halliday, A.N., 2009. Fractionation of oxygen and iron isotopes by partial melting processes: implications for the interpretation of stable isotope signatures in mafic rocks. Earth Planet. Sci. Lett. 283, 156–166.
Wood, B.J., Bryndzia, T., Johnson, K.E., 1990. Mantle oxidation state and its relationship to tectonic environment and fluid speciation. Science 248, 337–345.
Woodland, A.B., Koch, M., 2003. Variation in oxygen fugacity with depth in the upper mantle beneath the Kaapvaal craton, Southern Africa. Earth Planet. Sci. Lett. 214, 295–310.
Woodland, A.B., Peltonen, P., 1999. Ferric iron contents of garnet and clinopyroxene and estimated oxygen fugacities of peridotite xenoliths from the Eastern Finland Kimberlite Province. Presented at the the P.H. Nixon Volume; Proceedings of the VIIth International Kimberlite Conference, Cape Town, pp. 904–911.

Woodland, A.B., Ross, C.R., 1994. A crystallographic and Mössbauer spectroscopy study of $Fe_3^{2+}Al_2Si_3O_{12}$-$Fe_3^{2+}Si_3O_{12}$, (almandine-"skiagite") and $Ca_3Fe_2^{3+}Si_3O_{12}$-$Fe_3^{2+}Fe_2^{3+}$ + Si_3O_{12} (andradite-"skiagite") garnet solid solutions. Phys. Chem. Miner. 117–132.

Woodland, A.B., Seitz, H.M., Peltonen, P., 1999. Light and transition element composition of garnet and clinopyroxene from eclogite xenoliths from the Eastern Finland Kimberlite Province. J. Conf. Abstr. EUG 10, 821.

Yamashita, K., Creaser, R., Jensen, J.E., Heaman, L.M., 1999. Origin and evolution of mid- to late-Archean crust in the Hanikahimajuk Lake area, Slave Province, Canada; evidence from U–Pb geochronological, geochemical and Nd–Pb isotopic data. Precambrian Res. 99, 197–224.

Yaxley, G.M., Green, D.H., 1998. Reactions between eclogite and peridotite: mantle refertilization by subduction of oceanic crust. Schweiz. Mineral. Petrogr. Mitt. 78, 243–255.

Yaxley, G.M., Berry, A.J., Kamenetsky, V.S., Woodland, A.B., Golovin, A.V., 2012. An oxygen fugacity profile through the Siberian Craton - Fe K-edge XANES determinations of $Fe^{3+}/\Sigma Fe$ in garnets in peridotite xenoliths from the Udachnaya East kimberlite. Lithos 140-141, 142–151.

Zack, T., Foley, S.F., Jenner, G.A., 1997. A consistent partition coefficient set for clinopyroxene, amphibole and garnet from laser ablation microprobe analysis of garnet pyroxenites from Kakanui, New Zealand. Neues Jahrbuch Fur Mineralogie-Abhandlungen 172, pp. 23–41.